Acknowledgements

This work is supported by the George I. Alden fellowship, an endowed fund created by G. I. Alden to foster hydraulic research at Worcester Polytechnic Institute. I would like to thank W. W. Durgin for his continuous support throughout the project. I would also like to thank D. J. Olinger and M. A. Demetriou, for their valuable assistance to the work. I would also like to acknowledge the precious guidance of B. Edilberti, B. Furhman and L. Riley.

TABLE OF CONTENTS

LIST OF FIGURES

LIST OF TABLES

NOMENCLATURE

α	Angle of Attack
b	Width
C_f	Skin Friction Coefficient
C_p	Pressure Coefficient $(p-p_\infty)/q_\infty$
c	Chord length
D	Drag
D_f	Percent Velocity Defect
δ	Boundary Layer Thickness
θ	Boundary Layer Displacement Thickness
f	Frequency, Hz
F	Force
Γ	Circulation Strength
L	Lift
κ	Rotation
l_τ	Characteristic Length
l^+	Length Unit
ν	Fluid Kinematic Viscosity
ν/u_τ	Viscous Length Scale
Π	Coles Profile Parameter of Boundary Layer
Re_x	Reynolds Number with respect to the x direction
Re_θ	Momentum Thickness Reynolds Number

ρ	Fluid Density
q	Dynamic Pressure
θ	Momentum Thickness
τ_ω	Wall Shear Stress
t	Thickness
T_a	Actuation Time
u^+	Non-dimensional Velocity Unit
u_τ	Wall Friction Velocity
u_{rms}	Root Mean Square Velocity
u'_{rms}	Mean Velocity Fluctuations
u_τ	Characteristic Velocity, Friction Velocity
U	Mean Velocity
U_c	Convection Velocity
U_d	Velocity Defect
U_∞	Free Stream Velocity (Test section velocity)
ω	Frequency ($2\pi f$)
w	Displacement
y	Height
y^+	Wall Unit, y direction
z^+	Wall Unit, z direction

1. INTRODUCTION

Control of aircraft aerodynamics is an important application of microsystems technology. A small percentage reduction in drag can render a decrease in fuel consumption. In turn, the loss in fuel weight will reduce fuel and operating costs.

Next generation aircraft will require more microsensor capabilities, in areas such as position measurement, integrated flight and propulsion systems and radar/infrared technology. Advances in smart and distributed intelligence will add new requirements on sensor performance and reliability (Prosser, 1993). Particularly, the sensing and control of external aerodynamics will require development of sensors, actuators and computing capability. The goal of this work is to investigate the effect of a flap type actuator on boundary layer flow using an array of sensors to detect velocities. Understanding this effect will facilitate future use of Micro-ElectroMechanical Systems (MEMS) along with active control to reducing airfoil and fuselage drag.

With the exception of flow near stagnation points and portions of flow over wings, most of the airflow consists of turbulent boundary layers. Drag in turbulent flow has been observed to be partially produced by a process similar to instabilities that occur in boundary layers, both turbulent and transitional. This process is the turbulent bursting process. Past studies have resulted in two different portrayals of the turbulent process. The descriptions are primarily alike, however, the beginning of the process is slightly different. The first involves two counter-rotating streamwise vortical structures, located at the outer edge of the boundary sublayer, that transport the momentum from the wall to the fluid. The vortices bring slow moving fluid away from the wall, otherwise known as streaks. As the vortices grow in amplitude, they slowly move

towards each other. The growth of the streaks induces an inflection in the mean velocity profile. As the intensity grows, the upward moving fluid strengthens and an ejection occurs. At this point, the drag and shear stress is the highest because the high-speed fluid on the other side of the vortices is flowing down towards the wall. As the streaks continue to grow in amplitude an instability occurs and self-induction rapidly moves the vortices to the outer portion of the boundary layer. Due to a large energy transfer here, the vortices grow weaker. The last step in the bursting process is a rush of high-speed flow moving down towards the wall that washes the wall clean. This is called a sweep (Lumley and Blossey, 1998).

Other data have shown that the first step in the turbulent bursting process is not the counter-rotating streamwise vortices, but a horseshoe shaped vortex. The vortex is stretched by the flow and lifts the tip of the vortex into higher velocity regions, bringing momentum from the wall to fluid in the outer boundary layer. The streaks are generated inside of the hairpin vortex. Nonetheless, because movement away from the wall occurs slowly, there is a local deceleration of fluid at the wall. The ejection process transports low-momentum fluid away from the wall thus increasing the shear stress at the wall. Subsequently an influx of high-speed fluid, called a sweep, rushes at a small angle downward to the wall region to fill the empty space. This bursting mechanism increases the rate of momentum transport from the wall to the fluid and subsequently increases the amount of drag (Dahm and Diez-Garias, 2000). These two descriptions are quite similar. Some studies have shown that the counter-rotating vortices are the legs of the hairpin, otherwise called horseshoe, vortex.

The ultimate goal of researching turbulent bursts is the control of these turbulent bursts, which would ultimately reduce drag. For example, because an increase in shear stress has been found to occur when the vortex is created, a shear sensor could be used to sense the on-set of the bursting process, to detect the rise in shear stress in the outer side of the streamwise vortices. The sensor response to the increase in shear stress could be used for active control such as sucking or blowing the burst away from the airfoil.

This present work focuses on the controlled generation of the bursts both in the laminar boundary layer and the transition region. A piezoelectric actuator was used to disturb the sublayer flow creating burst-like disturbances whose effect was measured using an array of eight hot-wire sensors.

2. BACKGROUND

The following section presents background information essential to understand turbulence control strategies. It begins with a discussion of the fluid dynamics called aerodynamics; the study of the motion of air about a vehicle and the prediction of the forces it produces. The report continues with a description of laminar and turbulent boundary layers and the turbulent instabilities that occur within the boundary layer. Previous studies of the instabilities that occur in the turbulent bursting process are discussed followed by descriptions of the instrumentation employed for detection and control.

2.1. Aerodynamics

Aerodynamic resistance of streamline shapes arises primarily from the shear stress distribution over the body surface and induced drag due to finite span. The shear stress is due to the friction between the body and the air and is proportional to the viscosity, m, of the air and the slope of the velocity profile of the wall, $\partial u/\partial y\big|_0$. The resultant force can be split into two components: lift, L, and drag, D. Lift is the factor perpendicular to the free stream velocity, and drag is the component parallel to the free stream velocity (Anderson, 1991).

Because of cross-stream mixing, turbulent boundary layers have higher profile slopes at walls than laminar boundary layers. Much of the mixing and hence the skin friction drag due to the shear stress is the result of the bursting process.

One of the major operational costs of airliners is fuel. When the drag forces are high, more fuel is needed to propel the aircraft forward. Adding more fuel to an aircraft increases the weight of the aircraft, which also requires use of more fuel because of increased induced drag. The price of fuel oil has been increasing and is forcing the airliners to increase the price of tickets. If methods of controlling turbulent bursts can be developed so that drag is reduced then the amount of fuel, the weight of the aircraft and thus the price of commercial airline tickets will decrease while the range of flight increases.

Because turbulent bursts occur randomly in space and time, it is desirable to be able to initiate bursts at specific locations on command for research and development purposes. This desire defines the goals of the present work: to be able to create turbulent bursts on command. If turbulent bursts can be easily created, they can be studied in greater depth.

2.1.2. BOUNDARY LAYERS

The boundary layer concept reflects the physical fact that viscous effects are confined to thin layers adjacent to surfaces. Boundary layer flow may be laminar or turbulent depending on the Reynolds number and pressure gradient. Transition from laminar to turbulent flow depends on pressure gradient, surface roughness, body forces, heat transfer, and freestream disturbances (Fox and McDonald, 1992). However, we will be primarily concerned with flat plate or zero pressure gradient boundary layers.

Boundary layers develop over surfaces, such as over airfoils, ship hulls, and even atmospheric flow over land. Figure 2.1 represents boundary layer flow over a

smooth flat plate. The flow begins as laminar at the leading edge. Transition follows until the flow becomes turbulent. The flow can be characterized by the Reynolds number, Re_x, a ratio of length of the plate, x, speed of the flow, U, and fluid property, kinematic viscosity, υ. Transition for smooth places typically occur at Reynolds numbers greater than 2×10^6.

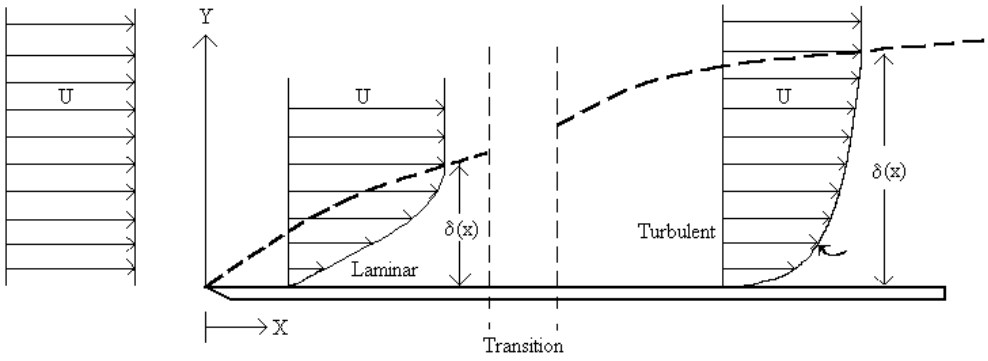

Figure 2.1. Sketch of Boundary Layer Flow.

The thickness of a boundary layer is measured from the surface to a location where the velocity is within one percent of the freestream velocity, $\delta = 0.99U$. Viscous forces slow down the flow and thicken the boundary layer. The boundary displacement thickness, δ^*, is the distance from the surface to the freestream velocity that that would be displaced if the flow were frictionless, to yield the same mass flow deficit (Fox and McDonald, 1992). The boundary displacement thickness is defined as $\delta^* = \int_0^\delta \left(1-\frac{u}{U}\right)dy$.

In 1908, Blasius found the solution for the incompressible, zero pressure gradient, laminar boundary layer using the governing equations of motion. At the wall,

the velocity is zero, as the distance from the surfaces approaches infinity, the velocity is equal to the freestream velocity. The continuity and momentum equations for laminar flow are:

$$\frac{\partial u}{\partial x}+\frac{\partial v}{\partial y}=0 \tag{2.1}$$

$$u\frac{\partial u}{\partial x}+\frac{\partial u}{\partial y}=\upsilon\frac{\partial^2 u}{\partial y^2} \tag{2.2}$$

By nondimensionalizing the equations with the boundary-layer thickness and velocity, Blasius was able to find a similarity free stream solution for the boundary conditions of no slip at the wall and asymptotic approach to free stream velocity away from the wall. Evaluating the equations for $u/U = 0.99$, the following approximations for the boundary-layer thickness, wall shear stress, and the skin friction coefficient were found. The skin friction coefficient is the wall shear stress over the dynamic pressure, $q=\frac{1}{2}\rho U^2$ (Fox and McDonald, 1992).

$$\delta \propto \sqrt{\frac{\nu x}{U}} \approx \frac{5.0}{\sqrt{U/\nu x}} = \frac{5.0x}{\sqrt{\mathrm{Re}_x}} \tag{2.3}$$

$$\tau_\omega = \frac{0.332\rho U^2}{\sqrt{\mathrm{Re}_x}} \tag{2.4}$$

$$C_f = \frac{0.664}{\sqrt{\mathrm{Re}_x}} \tag{2.5}$$

As the Reynolds number increases, the laminar flow becomes unstable and moves towards transition. Surface roughness and freestream disturbances may alter the transition location. Typically, however, it occurs at a Reynolds number greater than

2×10^6. The skin friction coefficient is less when laminar flow is maintained as long as possible. Subsequent to the transition region is the turbulent boundary layer, which has more across-stream momentum transfer than the laminar boundary layer (Fox and McDonald, 1992).

Turbulent boundary layers in equilibrium consist of three distinct layers: the inner layer, the outer layer and the overlap layer. Cross-stream transport of momentum from the wall to the fluid is caused by both molecular diffusion and velocity fluctuations (Dahm and Diez-Garias, 2000). The inner layer is the layer closest to the wall and ranges from $0 < y^+ < 30$, where y^+ is defined below. Within the inner layer, there are two more sublayers, the viscous sublayer, $0 < y^+ < 10$, and the buffer layer, $10 < y^+ < 30$. At the wall, where $y = 0$, there is no velocity and therefore no turbulent transport. A little distance from the wall, between $0 < y^+ < 10$, the flow is nearly laminar. Turbulent transport is minimal and molecular transport dominates. As the distance from the wall increases, $10 < y^+ < 30$, momentum flux density occurs, due to increase in molecular transport.

Within the inner layer, the shear stress, τ, where $\tau = \mu \left| \frac{\partial u}{\partial y} \right|$, remains constant.

The wall shear stress is given by the following equation.

$$\tau_\omega = 0.0233 \rho U^2 \left(\frac{\nu}{U\delta} \right)^{1/4} \tag{2.6}$$

The inner layer is scaled with the shear stress, τ_w, the kinematic viscosity, ν, the density, ρ, and the height, y. Four non-dimensional parameters can be used to characterize the

inner layer. These parameters include wall units, l_τ, y^+, u^+, and a characteristic velocity, u_τ. These parameters are defined as follows:

$$l_\tau \equiv \frac{\upsilon}{u_\tau} \tag{2.7}$$

$$y^+ \equiv \frac{y}{l_\tau} \tag{2.8}$$

$$u^+(y^+) \equiv \frac{u}{u_\tau} \tag{2.9}$$

$$u_\tau \equiv \left(\frac{\tau_\omega}{\rho}\right)^{1/2} \tag{2.10}$$

In the outer layer, where $y^+ > 30$, turbulent transport dominates. The velocity profile varies with the boundary layer thickness, $\delta(x)$, and with the streamwise pressure gradient, dP/dx. The desired pressure gradient over a flat plate is either a zero gradient or a positive gradient. If the pressure gradient is negative, separation will occur at or near the leading edge of the plate.

The overlap area is located in between the inner layer and outer layer, where the velocity profile is a logarithmic function. This area is otherwise known as the logarithmic layer.

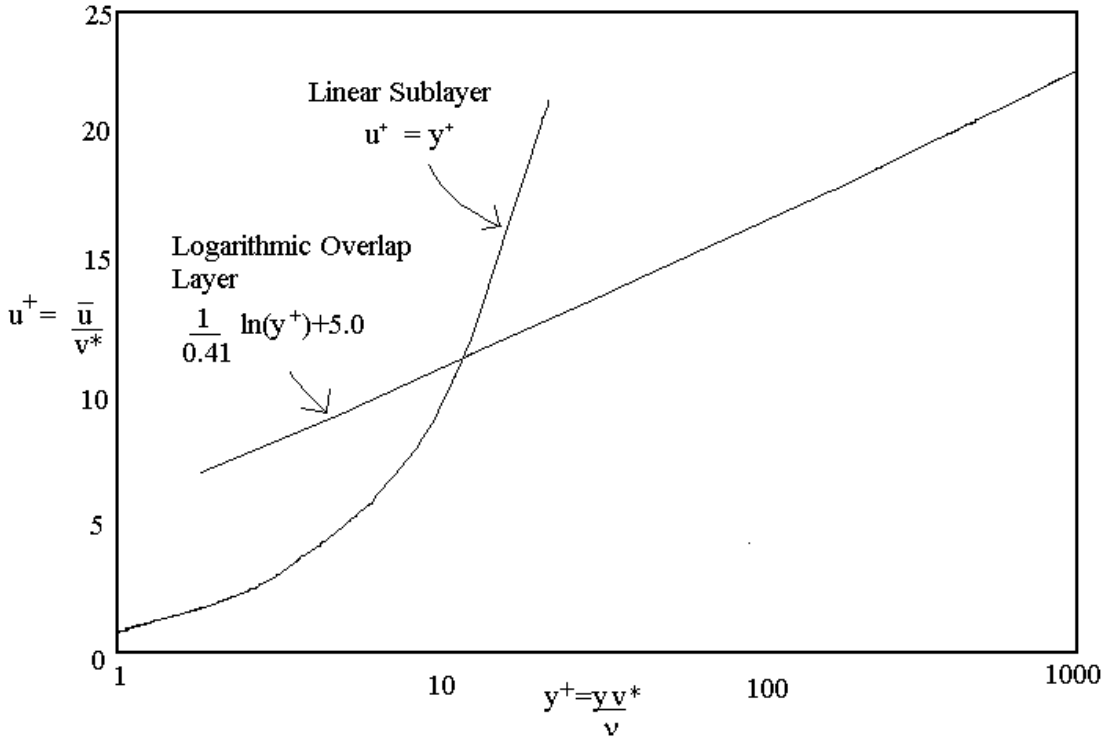

Figure 2.2. Sketch of Inner Wall Turbulent Boundary Layer.

For turbulent flow, the boundary layer thickness can be estimated by the following equation, assuming that $\delta = 0$ at $x = 0$, which is equivalent to assuming turbulent flow from the leading edge.

$$\delta = \frac{0.382x}{\mathrm{Re}_x^{1/5}} \tag{2.11}$$

Often times, when working with laboratory scale flows, the smallness of the Reynolds number results in excessive regions of laminar flow. Because of this, it may be necessary to have a boundary layer trip when conducting experiments. Tripping is usually implemented with rough sandpaper, small across stream ridges or rows of small tacks.

2.1.3. TURBULENT SUBLAYER VORTICES

Experimental evidence shows a dependency between the wall region and the outer region in turbulent boundary layers. The supporting facts are as follows. There is a distinction between smaller-scale active motions and large-scale inactive motions in the wall region. The large-scale motions scale with outer variables. The convection velocity of the larger-scale motions in the wall region, which can be approximated by $0.8U_o$, is larger than the local mean velocity. And finally, the average bursting period, T_B is more or less constant across the boundary layer; it scales with outer variables $U_o T_B/\delta \cong 5$, it has the same order of magnitude as the average period of the outer interface of the boundary layer (Hinze, 1975).

In the wall region of turbulent boundary layers, a progression of ordered motions, called the bursting process, dominates. The bursting process was first discovered in the late 1950s and continues to be intensely studied (Gad-el-Hak and Hussain, 1986). The turbulent bursting process is perceived with apparent recognizable average spacing in the spanwise and streamwise directions (Hinze, 1975). It is an important phenomenon to study because sweeps and bursts appear to account for most of the turbulent production (Offen and Kline, 1975). Two interpretations of the turbulent bursting process have been hypothesized from evidence scientists have found in the past. In the first, the process begins with a pair of elongated, streamwise vortices, with opposite circulations that lift slow moving fluid away from the wall. In the second, the process begins with the lifting of a coherent vortex structure, a hairpin vortex. Figure 2.3 is a sketch of the two different explanations. Both analyses agree

that flow patterns near the wall suggest a quasi-cyclic process that repeats in space and time, but not periodically at one specific instance, neither in time nor in space.

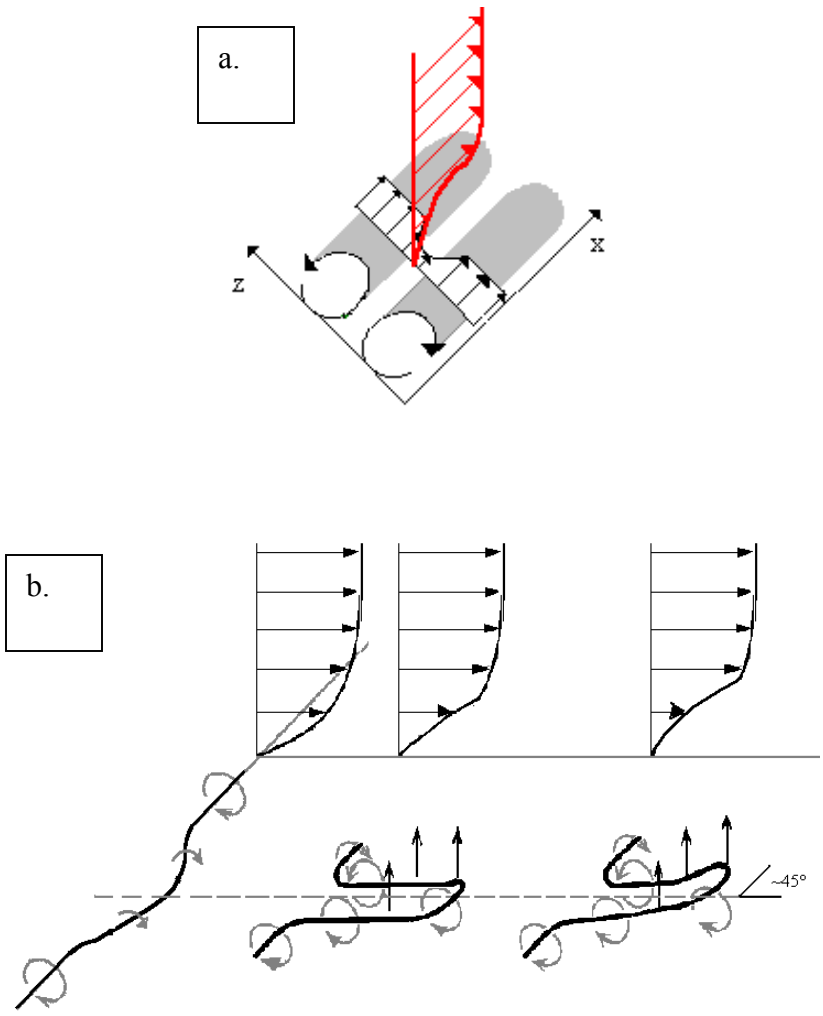

Figure 2.3. (a) Sketch of counter-rotating vortices. **(b)** Sketch of hairpin vortices.

In the viscous sublayer, the linear velocity distribution remains constant until the vorticity layer reaches a thickness where it becomes unstable. Disturbances cause the uniform vorticity layer to develop spanwise instabilities. Amplification and non-linear

growth of the instabilities lead to vortical structures, which group in pairs (Dahm and Diez-Garias, 2000). These elongated counter-rotating streamwise vortices seem to have radii between 20 υ/u_τ and 50 υ/u_τ, where υ/u_τ is the viscous length scale, υ is the kinematic viscosity, and u_τ is the friction velocity (Blackwelder and Haritonidis, 1983).

The vortices have an average spanwise wavelength of approximately 80-100υ/u_τ) and seem to lay parallel to and close to the wall (Gad-el-Hak and Hussain, 1986). They have been observed to appear as unequal pairs and can sometimes be found singly in the flow. Due to the direction of the vortices, a low-speed streaks forms between them and removes the low speed fluid from the wall rapidly ejecting it to the outer layer of the boundary layer, which can be seen from Figure 2.1.a, and a high-speed streak is produced by the downdraft of the vortices on the opposite side (Lumley and Blossey, 1998). Since the streamwise vortices transport the momentum from the wall to the fluid a large amount of drag is created.

Streaks seem to ordinarily have a width of 10-20υ/u_τ and a length of 100-1000 υ/u_τ. Because of their narrowness, Corino and Brodkey showed that there is significant shear in the spanwise direction (Gad-el-Hak and Hussain, 1986). Shortly after, the streaks are lifted away from the wall and induce an inflection in the velocity profile, during what is called the ejection process, they seem to oscillate. Within a short timescale, the amplitude and scale of this motion seems to grow larger until it breaks down and chaotic motion is left. Energy is transferred from the large to small scales producing fluctuations. This is called the 'burst'. This bursting process transports the momentum from the inner layer to the outer layer at a much faster rate than diffusion

and therefore is effective at dissipating energy. Because of this increase in transport from the wall to the fluid, turbulent boundary layers produce high drag (Dahm and Diez-Garias, 2000). Pressure fluctuations are generated from the presence of turbulence as well as the wall shear stress, which is the highest during a 'burst'.

Following the burst, a sweep motion, consisting of high-speed fluid, from the outer flow field, washes away the chaotic motion from the near wall region. This sweep motion seems to scale with δ and U_∞ of the outer flow (Blackwelder and Haritonidis, 1983). Figure 2.4, reprinted with permission from Cambridge University Press from the Journal of Fluid Mechanics, represents the start of the bursting process due to instabilities in the two counter-rotating vortices that lead to low speed streaks.

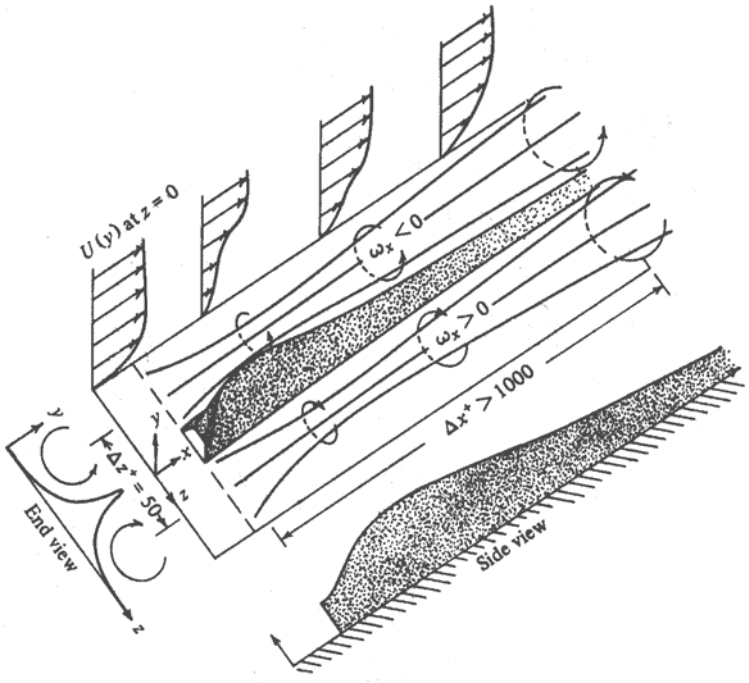

Figure 2.4. Conceptual model of the counter-rotating streamwise vortices (Blackwelder and Kaplan, 1976).

At times, this process resembles the laminar turbulent transition region. This bursting cycle description does not have a definite beginning, so this description begins when a horseshoe vortex is beginning to develop in the inner region near the wall, due to a large-scale disturbance in the outer region.

The second description of the turbulent bursting sequence has many similarities, but varies in that the predominant coherent structure in the process is the hairpin vortex and not the counter-rotating streamwise vortices. The flow bends the vortex in the streamwise direction into an elongated U-shaped loop. Self-induction moves the tip of the vortex away from the wall and into faster velocities.

The stretching increases the vorticity and creates an outward flow between the legs of the U-shaped vortex with a strong u_2-component near the tip. Because the vortex is slowing, moving away from the wall, there is a local deceleration of fluid at the wall. Visualization and numerical results have shown that the hairpin vortices have approximately 45° inclination (Gad-el-Hak and Hussain, 1986). Different investigators have found slight variations in inclination.

The ejection process transports low-momentum fluid away from the wall thus increasing the shear stress at the wall. At $x_2^+ = 5$ to 30, a strong horizontal shear-layer is formed, showing as an instantaneous U_1-velocity profile dent with inflection points in data. Local variational instability and breakdown of the flow surround the original vortex tip makes a turbulent burst. The turbulent burst creates pressure waves, which propagate through the whole boundary layer. Fluid of high turbulent intensity is pushed downstream and moves farther away from the wall, increasing in scale by turbulent diffusion. At the same time high-momentum fluid is entering from the flow upstream,

the high turbulent intensity fluid is swept downstream. Movement of fluid towards the wall results in a sweep. This rush of fluid into the wall has already begun when a negative y-velocity component has already begun to breakdown. The sweep is higher momentum fluid almost horizontal in direction. Both the ejection process and this inrush of fluid add to the high shear stress and turbulence in the region of $y^+ = 10$ to 15 (Hinze, 1975). Figure 2.5, reprinted with permission from McGraw-Hill, shows a conceptual image of the horseshoe vortex progression.

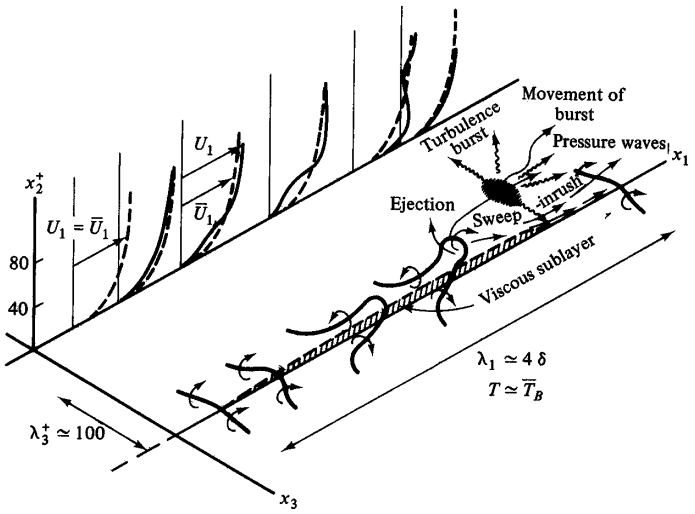

Figure 2.5. Conceptual image of horseshoe vortex in bursting cycle (Hinze, 1975).

Investigators have found experimental results supporting both descriptions of the bursting process. The important purpose is that in both processes, the main differentiating factor is the lift off of the wall. Offen and Kline (1975) hypothesize that the difference between the transverse vortex and the stream wise vortices may come from the location of the probes, hydrogen bubbles or smoke that are typically used to study such flows. If the plane cuts the center or tip of the stretched vortex, a transverse

vortex will show, however if the probes pass through the legs of the hairpin vortex, upwards-tilted streamwise vortices will show (Offen and Kline, 1975). This has been sketched in Figure 2.6.

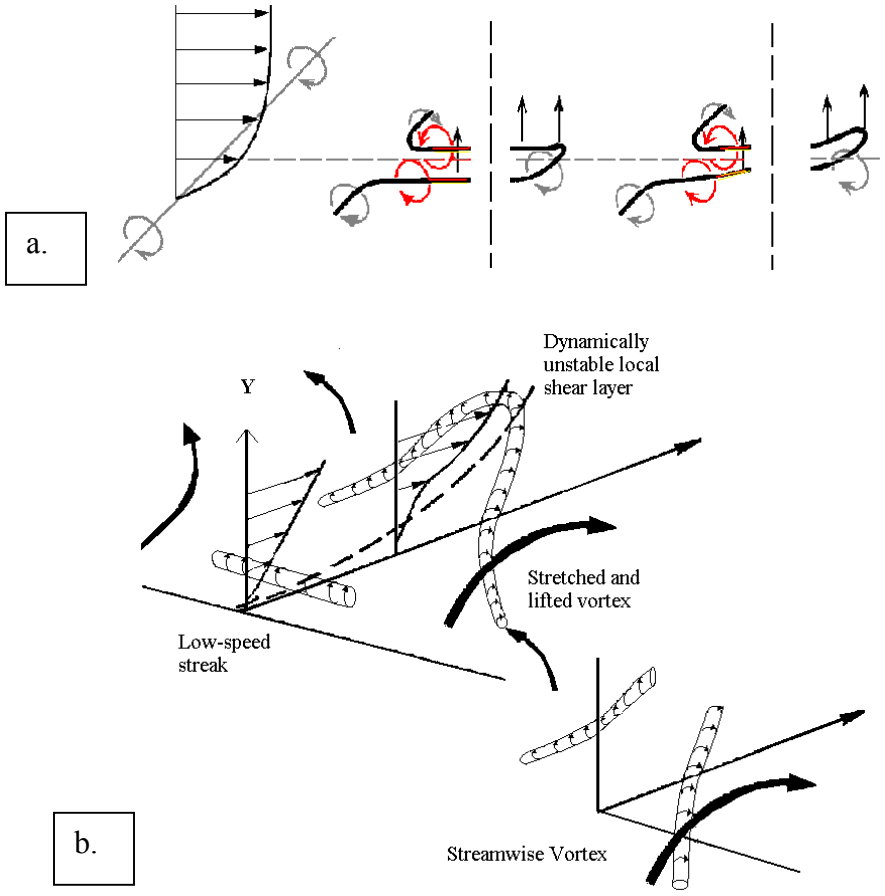

Figure 2.6. (a) Hairpin Vortex cut to show counter-rotating vortices. **(b)** U-shape streak break-up cut to show streamwise streaks.

Even after fifty years of study, there exist more questions that need to be answered. Future studies should try to answer questions such as the origin of these structures, whether the longitudinal vortices are the legs of hairpin vortices, determination of the exact geometries of the vortices, and the evolution of the exact

angle of inclination of the hairpin structures. Being able to generate turbulent bursts on demand would greatly facilitate the study of turbulent bursts.

Years of investigation have allowed us to describe the bursting process because of the information obtained using various methods of detection. The methods can be roughly categorized into visualization and probe methods. Both methods have advantages and disadvantages, but none have been able to study the complete structure of turbulent bursts.

Various visualization techniques used in past studies occur either in liquid or air. In water, examples of techniques used include dye, illuminated particles, and hydrogen bubbles. In air, smoke visualization has been used.

Methods of detection using probes are limited due to the size of the eddy structures in turbulent bursts. Such methods include Constant Temperature Anemometry (CTA) such as hot-wire, flush mount and invasive hot-film. Additionally, pinhole pressure transducers have been used. The work described herein, hot-wire anemometry, was used to sense burst-like structures.

2.2. SENSORS

2.2.1. METHODS OF DETECTION

Hot-Wire Anemometry dates back to the beginning of the 20th century where, according to King (1915), preliminary experiments were carried out by Shakespear at Birmingham in 1902. The work did not progress due to the difficulty of calibrating the wires. In 1914, 1915 and 1916, King is known to have created the basic design of hot-wire anemometers and developed the theory of heat convection from heated cylinders

immersed in a stream of fluid. In 1927 Simmins and Bailey described the two fundamentally different thermal anemometry methods; constant current and constant temperature. In the constant current method, the heating current through a hot-wire is kept constant. The changes in the wire resistance reflected the velocity of the flow. In the constant temperature method, the resistance is kept constant using a Wheatstone bridge, which is kept balanced by adjusting the heating current. In this case, the current needed to maintain constant resistance was adjusted only slowly so that it was a measure of mean velocity (Comte-Bellot, 1976).

In later years, the focus of thermal anemometry turned towards measuring the velocity fluctuations in a flow. In 1929 Dryden and Kuethe developed an electronic technique that was used in conjunction with the constant current method explained above. Ziegler, in 1934, applied feedback to the constant resistance method to maintain the constant wire resistance at all times. Soon after, the research focused on improving the electronics to obtain velocity fluctuations, and mass flux (Comte-Bellot, 1976). These early works lead the way for anemometry to evolve to its present state.

A hot-wire sensor can be a thin metallic wire, usually soft soldered to two prongs and can be etched to a certain effective length. When probes are made of bare wires, they are electrically soldered onto the prongs. Materials for hot-wire sensors are usually platinum, tungsten or platinum-rhodium or iridium.

A hot-film sensor is usually a thin film of platinum deposited by sputtering on a quartz substrate. A quartz coating can be applied to protect the film from electrochemical effects (Comte-Bellot, 1976). Hot-film sensors can be fabricated as flush wall sensors that primarily reflect shear stress.

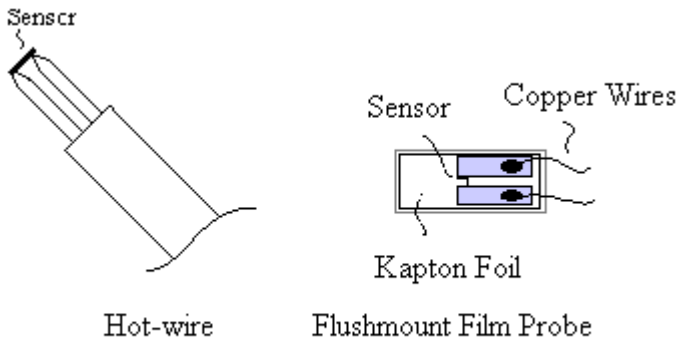

Figure 2.7. Hot-wire and Flushmount Film Sensors.

Flushmount film sensors are useful for measuring wall shear stress, heat flux or flow separation. Typical materials used are platinum film on quartz substrate, which provide stable anticorrosive film materials, a high strength and low thermal conductivity. There is also an aluminum coating for air applications that have high abrasion resistances. There are sensors with no coatings, which are useful for non-conducting liquids (www.dantectmt.com).

Traditionally, hot-wire sensors have been more widely used in thermal anemometry. The wire sensor is better in measuring turbulence fluctuations because higher frequency response can be obtained. Platinum and tungsten wires are the most frequently used type of hot wire. Tungsten is strong and has a high temperature coefficient. At high temperatures in oxidizing atmospheres, such as air, it deteriorates. Platinum wires are a bit weaker, but can be fabricated in smaller sizes and withstand the high temperatures in oxidizing atmospheres (www.tsi.com).

The typical arrangement of a hot wire is normal to the flow, which obtains the longitudinal velocity component. If the probe has two wires, forming an "X, " which

are used to obtain the longitudinal and transverse velocity components, it must be oriented with the split facing upstream. There are also three wire probes, to measure all three velocity components. The wire is soldered to the needles at an orientation 35.26° (www.tsi.com). Figure 2.8 shows the orientation of a single hot-wire sensor to the flow.

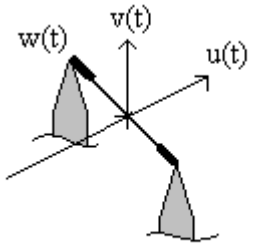

Figure 2.8. Orientation of a Single Hot-wire Sensor to the Flow.

King's Law is the foundation of hot-wire calibrations. It states that a cylinder of infinite length can approximate a fine wire, mounted between two needles. If the wire is placed perpendicular to the freestream flow, and is held at a constant temperature, then the current passing through the wire can be a measure of the velocity, U, by the following equation, where a and b are constants found through calibration. It is based on an empirical heat transfer formula and the electrical power dissipated (White, 1974).

$$I^2 = a + bU^{1/2} \tag{2.12}$$

The constant anemometer system that controlled the hot-wire probes in this work was an eight channel IFA 300 Anemometer system. It uses a Wheatstone bridge, as most anemometer systems do, to maintain the operating resistance of the sensor. In this application, a standard bridge with 10 ohms was used, but for applications with higher power needs, a bridge with 2 ohms can be used. When the fluid flows over the

sensor, heated to a certain temperature, the internal amplifier senses the off-balance and adjusts the voltage to the bridge until it balanced once again. Since the bridge voltage is sensitive to temperature, there is a built-in thermocouple that reads the ambient temperature to correct the results. Figure 2.9 shows the basic circuitry of a single channel IFA 300 system.

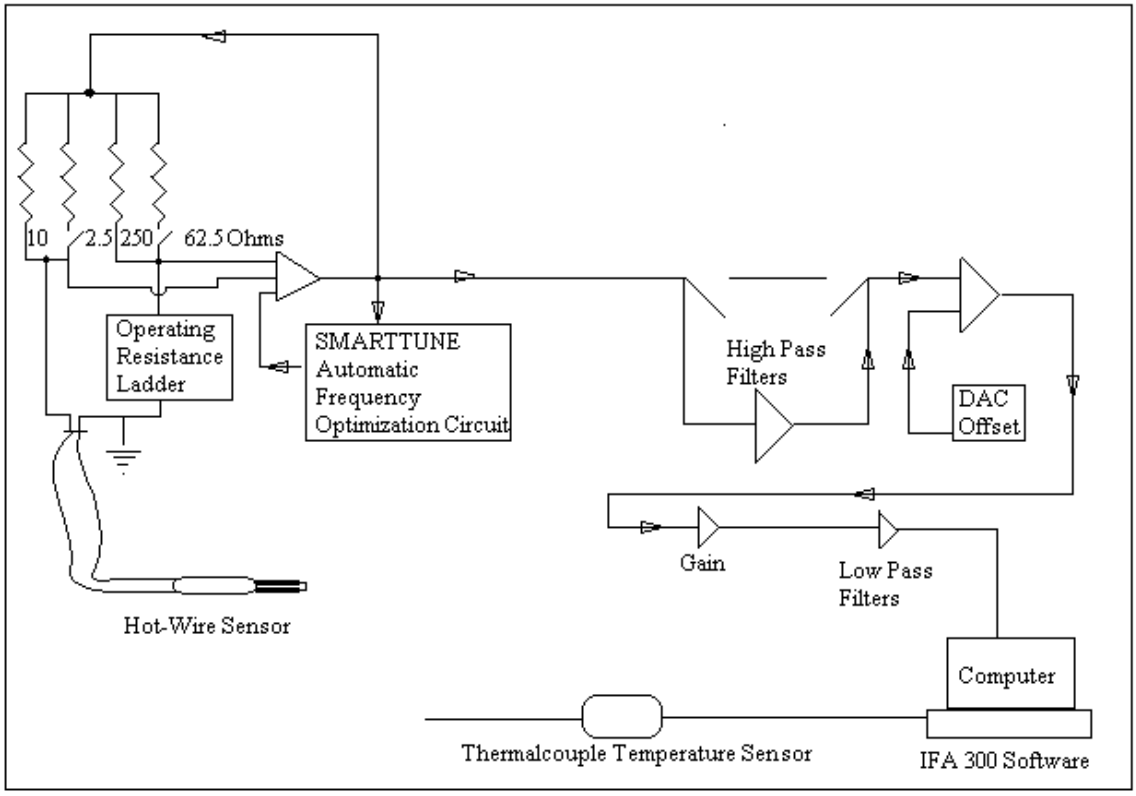

Figure 2.9. Circuitry of the IFA 300 Anemometer System.

Each unit has one microprocessor system board to control the functions and settings of the anemometer and signal conditioner. The microprocessor has a thermocouple circuit that can measure the temperature, and a 12-bit analog-to-digital converter to transfer the data. This system has a SMARTTUNE technology, which constantly checks the bridge voltage and feeds the signal back to the amplifier circuit.

Not only does this prevent system oscillations from occurring, but also it maintains the necessary frequency response that the sensor requires.

When velocity fluctuation measurements are needed, the signal conditioners supply filtering and increase the voltage gain to use the entire voltage range. An offset option is available when bridge voltage is greater than the 5 V range. The low pass filters remove high frequency signals that are not of interest (IFA 300 Instructions Manual).

2.2.3. PAST STUDIES

Since the 1950s, investigators have studied the turbulent bursting phenomenon using various methods. Initially, most information on the bursting process was found through visualization techniques. Examples of the past studies and their findings are included in the following section.

In the 1950s, Hama injected dye at the wall of a turbulent shear flow and observed that low-speed streaks occurred randomly in space and time. In 1959 Kline and Rundstadler experimented with the dye method and hypothesized that these streaks were connected to an organized three-dimensional vortical structure that existed in the near wall region. Kline et al. later confirmed this hypothesis in 1967 by studying the process using the hydrogen bubble method together with dye injection. These scientists and others suggested that the low-speed streaks preceded the bursting phenomenon, although the mechanism responsible for the process remained unclear (Blackwelder and Eckelmann, 1979).

In 1958, Grant was one of the first to obtain measurements using the invasive method of hot-wire anemometry. He found structures that resembled the structures of a burst. Bakewell and Lumley, in 1967, used space-time correlations in the wall region of a pipe flow and found that the velocities they measured seemed to match those of a pair of counter-rotating streamwise vortices. Laufer and Kaplan used a hot-wire rake and found that there are regions of high and low speed streamwise momentum during the bursting process.

In 1979, Blackwelder and Eckelmann studied turbulent bursts in an oil channel using flush mounted hot-film sensors to avoid physical probe interference in addition to a single velocity probe. Two flush hot-film sensors were arranged in a V-shape between which the single hot-film velocity probe was placed perpendicular to the hot-film probes and mounted at $y^+ = 15$. The Reynolds number in the oil channel was 7700. The experiments showed that the bursting process was a result of two counter rotating vortices that pumped low speed fluid away from the wall. The origin of the counter rotating vortices was unknown. The low speed fluid being pumped from the wall created a low-speed streak and an inflexional velocity profile, followed by the high-speed fluid, the sweep, flowing over the slow-speed streaks. This interaction seemed to destroy the counter rotating vortices. Because the sweep of the outer fluid triggered the burst, Blackwelder and Eckelmann conclude that the frequency of occurrence of the bursting phenomenon should scale with the other flow variables, δ and U_∞.

Blackwelder began a more detailed study of turbulent bursts with Haritonidis in 1983. They studied the dependence of bursting frequency on the Reynolds number and used various probe techniques to produce a better reproducibility. The experiments

were conducted in a wind tunnel with a flat plate in a Reynolds number range of $10^3 < U\vartheta/\nu < 10^4$. The flow was tripped into a turbulent shear flow by two staggered rows of inverted rivets and sheets of No. 24 carborundum metal cloth glued over the initial 56 cm of flat plate. Using hot-wire sensors less than twenty viscous length scales, they minimized spatial-averaging effects. Hot-wire probes in a rake formation were used at $y^+ = 15$. The probes were operated at overheat ratios of 33%, giving frequency responses of 5-12 kHz. The sensing length was chosen for an l/d ratio greater or equal to 200, and the temporal record length was taken to be $1000\delta/U_\infty$, which was equivalent to the passing of several hundred large outer flow eddies. This experiment showed that the streamwise vortical streaks had a radius of (20 to 50)ν/u_τ and be (10 to 20)ν/u_τ wide, and (100 to 1000)ν/u_τ long.

In 1992, Morrison, Subramanian and Bradshaw studied the phenomenon at two higher Reynolds numbers in boundary layers with a zero pressure gradient. The experiments compared the process over a smooth wall layer versus a rough to smooth surface. When the boundary layer developed on the smooth wall, ejections and sweeps, two stages of the bursting process, were present and seemed to be responsible for the turbulent energy production. When the boundary layer in the rough to smooth surface, the ejections and sweeps were not near a condition of energy equilibrium. They concluded that sweeps seem to be a mirror image of ejections about the line joining the centers of the vortices.

In 1994, Blackwelder and Myose studied the laminar flow over a concave wall, which creates counter-rotating streamwise vortices, Goëtler vortices. The experiment was conducted in a wind tunnel. The air flowed over an oscillating airfoil that was

powered by a stepping motor and into the concave wall test area. The instabilities produced were similar to a moderate Reynolds number turbulent boundary layer. Wall eddy breakdown was triggered by streamwise acceleration in the outer layer of the turbulent boundary layer. The eddys can break down alone, however interacting with the outer layer slowed down the break down process. The studies showed that the outer region of turbulent boundary layers affects bursts. The instrumentation used was constant temperature anemometry (CTA). A ten-wire y-rake supported hot-wire sensors, operated at a 20% overheat. In addition to this invasive technique, the two scientists also used the smoke wire technique for flow visualization. The smoke wire was located at $x = 22$ cm and $y = 0.14$ cm ($y/\delta_{blasius} \sim 0.35$).

In 1996, Coughlin and Marcus conducted a numerical study of the flow between two concentric rotating cylinders in which the structure alternated between laminar and turbulent. This study confirmed results from an experiment by Hamill *et al.* that bursts are a temporal oscillations between a spatially laminar and turbulent flow; it proved that the onset of turbulence due to these linear instabilities. The calculations showed that once an "interpenetrating spiral" flow began, the turbulent bursts began. The studies found that small scales of the burst are efficient at dissipating energy, and is a good method of detecting the presence of a turbulent burst. The viscous dissipation is at a maximum when the burst peaks, and drops when the burst collapses.

Both passive and active control methods have been used to control the turbulent bursting process. Small surface riblets are the primary passive control method at this time. They are used to prevent the streamwise vortices from bringing high momentum fluid down to the surface. The riblets are effective only when the bursts are occurring.

Since the bursts are random in time and space, the riblets are otherwise increasing the drag. Active control methods, such as heating or cooling the wall on which the turbulent bursts pass over were seen in limited cases.

In 1998, Lumley and Blossey completed a direct numerical simulation of a turbulent channel flow with flat walls and a moving boundary. The moving boundary allows active control simulation. The simulation consisted of using an actuator to raise a bump under streaks lifting the high-speed fluid from the wall into the low-speed streak. Adding a body force to the code that induced counter-rotating vortices simulated the actuator. This motion resulted in 20 percent reduction in drag, while the flap was up, but when the flap was lowered, the drag increased. Raising the actuator caused the low speed streak to separate, but behind the bump, the flow rejoined itself and generated another strong vortex pair beneath the first, causing a more complicated flow.

More recently, attention has been focused on microelectromechanical systems (MEMS) for possible active control. Typically these systems incorporate shear stress or velocity sensors, a control system, and some system of actuation to disrupt burst formation.

Chih-Ming Ho *et al.* from the University of California and California Technical Institute have begun studies using micro-surface shear stress sensors in place of CTA for air because CTA is not as sensitive. Due to the small size of the microsensors, many can be placed on one wafer at a time. Microactuators can be used to control the bursting process or to create the bursting process. Faiz Sherman along with Chih-Ming Ho *et al.* used high-aspect-ratio large deflection in-plane microactuators about 500-800

μm in size. The electrostatically driven microdevices act as cantilever beams to displace the flow so as to avoid the creation of streaks that occur in the bursting phenomenon. One example is the MEMS "Bubble" actuators that break down the vortex symmetry of the streaks. Another example is when a silicon nitride flap driven by an electromagnetic field was set downstream of a vortex generator, a bump in the plate. When actuated, the upward motion showed transport of high-velocity fluid away from the wall. The downward motion of the flap reacted with the wall and pushed the flow upward. Overall, the motion of the actuator resulted in a lower skin drag coefficient than the stationary vortex pair. In reality, one microactuator will not have a great effect on drag; turbulent bursts are occurring everywhere. Many sensors and actuators are needed to control the flow. Ho *et al.,* is currently working to incorporate the microsensors, microelectronics, and microactuators onto one chip.

Tsao *et al.* use a combination of microsensors, microactuators and microelectronics to control turbulent bursts. Their ultimate goal combined the microsensors and microactuators onto one single wafer. The microsensor is a MEMS hot-film shear stress imager consisting of multiple rows of vacuum insulated shear stress sensors. Since the geometry of turbulent bursts varies with speed, the vortex pair decreases in size as the Re number of the flow increases, micromachining allowed the scientists to create four different sized microsensors. The mocrosensors successfully imaged turbulent bursts in a turbulent shear flow. The microactuator was a silicon flap with 30 turns of copper coil that matched the size of the vortex generator, which was 1.3 mm thick, located upstream. As the actuator oscillated, it generated perturbations in the flow, which changed the shear stress of the streaks and lessened the intensity.

Diez-Garias and Dahm proposed a method for controlling the bursting process by using a closed-loop feedback control. Their method utilized a local blowing or suction at the wall to displace the individual sublayer vortices. Figure 2.10 shows the displacement of a sublayer vortex by an array of individually addressable microactuators.

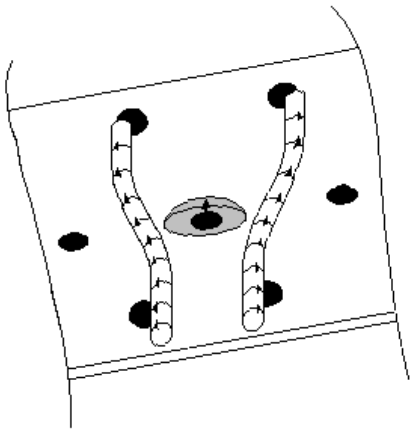

Figure 2.10. Representation of Sublayer Vortex Displacement by Blowing.

Other ideas include slot microactuators that could create alternating positive and negative volume displacements.

Instead of using active control to stop bursts, Gad-el-Hak and Hussain attempted to generate artificial bursts to be able to study them more systematically. They used two techniques to create the bursts, suction holes and a delta wing, which were visualized through florescent dye and hydrogen bubbles. Abrupt suction through one, two, three or four holes, with a distance of 100 wall units. The suction allowed a withdrawal of fluid and generated a horseshoe-type vortex that progressed into a burst. The delta wing had a span, b, of 80 wall units and laid flush on the plate. When the delta wing was pitched to a negative angle of attack of 30°, a hairpin-like vortical

structure, whose head lifted away from the wall was generated. Both methods were utilized in laminar and turbulent flow. Hot-film probes measured the instantaneous longitudinal velocity and successfully detected bursts and low-speed streaks when the generators were triggered. The artificial bursts are similar to natural bursts.

2.2.4. PIEZOELECTRIC ACTUATOR

In this work, a piezoelectric actuator was used to initiate bursts. Piezoelectric materials are solids, which generate a charge in response to a mechanical deformation, or alternatively, develop mechanical deformation when subjected to an electric field. They are employed as sensors and actuators in smart materials and structures. Some materials that have piezoelectric properties are quartz crystals and tourmaline, which are naturally piezoelectric synthetic ceramics, polymers and alumina nitride. Piezoelectric ceramic materials are typically employed as actuators while polymeric piezoelectric materials are typically employed as sensors for tactile sensing, temperature sensing, and strain sensing.

Figure 2.11 shows two cases of dipole arrangement in piezoelectric material. In Figure 2.11.a, the unstressed material is subjected to an electric field, while in Figure 2.11.b, the material has a zero field strength. As can be seen in Figure 2.11.b the material is expanding in the direction of the poling axis due to an applied negative voltage. If a positive voltage were applied, the material would contract.

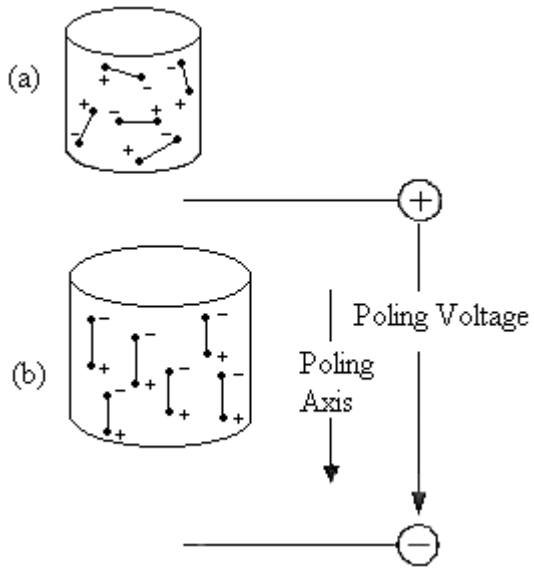

Figure 2.11. Dipole Arrangement of Piezoelectric Materials.

A bimorph actuator from Active Control Experts was used in this work. It consisted of two rectangular independent piezoelements stacked on top of each other. A power supply was connected so that one of the elements expanded while the other contracted, thus causing an out of plane bending motion. Since one end of the actuator was clamped, the free side could bend creating a cantilever motion as shown in Figure 2.12.

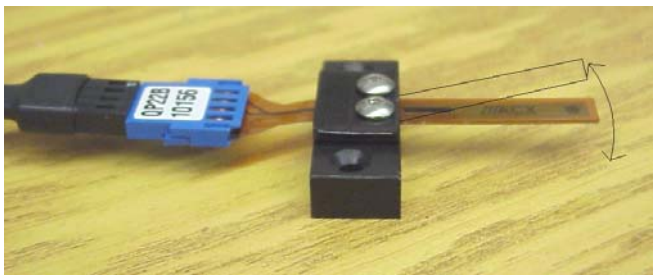

Figure 2.12. Clamped Bimorph Actuator.

Biomorph actuators have many advantages. They are small, light in weight, and do not require as much power as solenoid actuators. They are often used in pneumatic control valves, fluid pilot valves, switches, relays and pumps.

In choosing a design for a bimorph actuator, one must take into account the desired force, F and displacement, w. These parameters vary with length, l, width, b, and thickness, t.

$$F \propto b\frac{t^{'}}{l} \tag{2.13}$$

$$w \propto \frac{l^{'}}{t} \tag{2.14}$$

As the length of the actuator increases, the displacement increases, while the force decreases. As the width increases, the force increases, but the displacement is not really affected. As the thickness increases, the force and the displacement both decrease.

Another parameter to consider is the operating frequency. If an actuator operates at a higher frequency than its resonant frequency, then the force and displacement may be affected. A bimorph actuator is designed to have a resonant frequency that is three times higher than the highest operating frequency for a particular application. Altering the actuators geometry can change the frequencies. A shorter or thicker actuator has a higher frequency (www.acx.com).

A bimorph actuator can utilize various piezoceramic materials. Some materials may have a higher force per geometry, or can operate under higher frequencies. While other piezoceramic materials can remain energized for longer periods of time than others.

The bimorph actuator used in this work, has a standard actuating length of 0.75 inches and a width of 0.25 inches. When the device was poled with a positive voltage of 100 V and a current of 50 mA, the resulting maximum force was 0.41 ounces, yielding a maximum peak-to-peak displacement of 0.0105 inches. However, the clamp used in this work constricted less of the actuator, leaving an actuating length of 1.125 inches, in order to yield a slightly higher displacement of 0.0275 inches.

3. METHODOLOGY

3.1. EQUIPMENT

The wind tunnel used in the experiments is an AEROLAB Low Turbulence, low speed, open circuit wind tunnel. The nine fiberglass-reinforced plastic blade axial fan, powered by a 180 volt DC at 9.5 Amps and up to 1750-rpm motor, is used to create the flow field with airspeed ranges of 0 to 80 mph. The air flows through a 131 x 134 cm honey comb intake, with 0.7 cm cells, through a contraction ratio of 16:1 and into a test section with a cross sectional area of 12 x 12 inch and 45 inches in length. After exiting the test section the air makes two 90° turns before returning to the intake chamber.

Installed in the test section was a 34-inch x 11.531x 0.25-inch aerodynamically smooth flat aluminum plate. The leading edge of plate had a 45° angle. A boundary layer trip, consisting of a staggered row of 1.0 x 2.5 inch 220 grit sand paper was glued 0.25 inches from the leading edge for some tests.

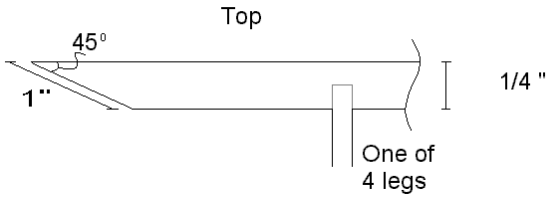

Figure 3.1. Flat Plate.

Tungsten platinum coated wires from TSI were used in an 8-sensor array to measure turbulent bursts. The diameter of the sensing area was 3.8 μm (0.00015

inches) and the length is 1.27 μm (0.05 inches). The maximum operating temperature was 300°C. An overheat ratio of 20% was used in the experiment.

The sensors were controlled by an 8-channel constant temperature anemometer system from TSI, called the IFA 300. Along with the constant temperature anemometer, data acquisition and analysis software and an A/D converter board were installed. The IFA 300 provides up to 300 kHz frequency response and has a built-in thermocouple circuit for measuring the fluid temperature and for making temperature corrections. The set-up, operations, probe calibrations and data acquisition are all software controlled by an RS-232 interface. The software itself runs on Microsoft Windows. The A/D converter board can plug directly into the PC. The measurements were taken over a 5.12 second time span. The data was take at 1000 points/channel with a frequency response was 200 Hz.

A constant temperature anemometer system consists of a bridge and an amplifier circuit that monitors a wire or film sensor. The system heats the sensor to a specific temperature. As the fluid flows past the heated sensor, the amplifier in the system senses the off balance of the bridge, the change in temperature of the sensor, and corrects the voltage to the bridge, rebalancing the bridge. The change in voltage is related to the velocity of the flow. Since the bridge voltage senses temperature and velocity, a built-in thermocouple can be used to measure the fluid temperature. The software then takes this reading and makes necessary corrections to lessen the effect of the fluid temperature on the sensor readings.

When Calibrating each hot-wire probe, the offset and gain settings must be determined. The offset and gain determine the resolution available from the A/D board.

When the values are found, they are applied to the Bridge Voltage, V_b, which acquires a range of the Output Voltage to be close to –5 to +5 VDC. The following equations are methods to finding the offset and gain for each hot-wire probe. A table of the offset and gains for each probe is located in Appendix A.

$$\frac{1}{2}(V_{b\min} + V_{b\max}) = Offset \tag{3.1}$$

$$\left[\frac{-4}{(V_{b\min} - Offset)}\right] \geq Gain \leq \left[\frac{4}{(V_{b\max} - Offset)}\right] \tag{3.2}$$

$$\left[(V_b) - (Offset)\right] \times Gain = OutputVoltage \tag{3.3}$$

The following table is a list of probes and their offset and gains calculated by equations (3.1), (3.2), and (3.3).

PROBE NUMBER	OFFSET	GAIN
14133	1.10645	~ 12
14134	1.10165	~ 12
14135	1.1114	~ 12
14136	1.11	~ 12
14137	1.10405	~ 12
14138	1.0967	~ 12
14139	1.08785	~ 12
14140	1.1114	~ 12
15153	1.1	~ 12
15154	1.12	~ 12

Table 3.1. Probe Offset and Gains.

The following graph is the Calibration curves for each probe after implementing the new offset and gains. Each probe must be calibrated separately in the wind tunnel.

The coefficients located at the upper-right corner of the calibration graphs fit into the following equation for velocity:

$$Velocity = K + AV_b + B(V_b)^2 + C(V_b)^3 + D(V_b)^4 \qquad (3.4)$$

PROBE NUMBER	K	A	B	C	D
14133	-30.2498	62.227	2.10247	-77.5752	45.5955
14134	-3.30733	-6.11628	48.7554	-74.7198	37.1424
14135	-9.02105	23.2508	-3.44125	-35.3531	26.2398
14136	-36.7641	121.781	-131.77	36.134	12.5911
14137	-13.5303	37.5711	-20.9997	-25.3835	24.0078
14138	-178.961	650.555	-857.62	473.413	-85.298
14139	-41.0604	138.143	-156.436	54.114	6.94331
14140	-75.3335	270.207	-344.877	172.378	-20.7496
15153	-48.8413	172.084	-208.469	86.6577	0.38599
15154	-33.908	116.212	-132.532	43.2343	8.69817

Table 3.2. Velocity function coefficients for probe calibration.

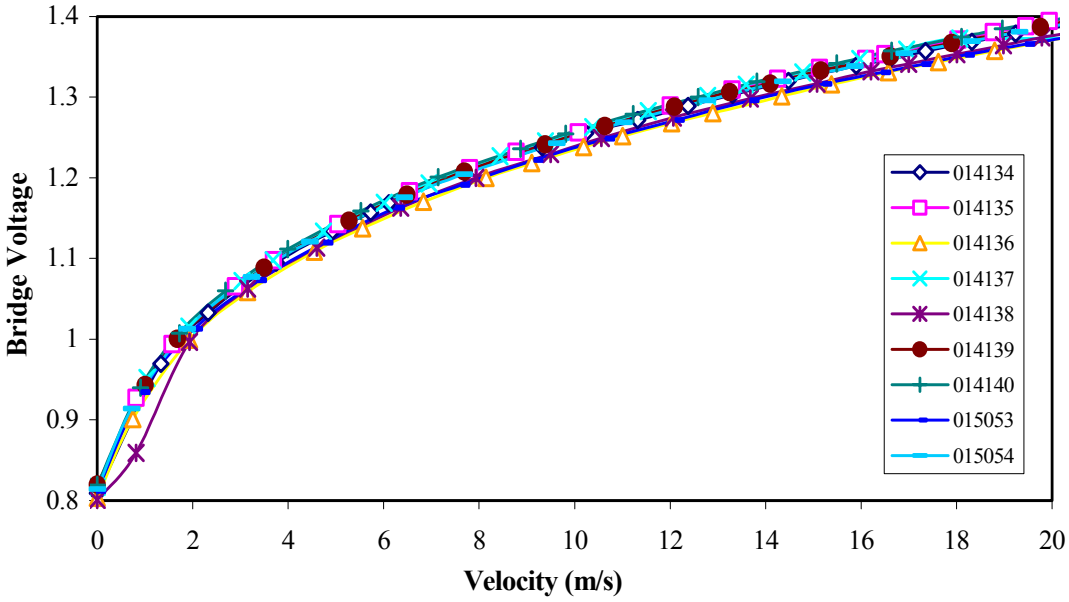

Figure 3.2. Probe Calibrations.

A 50 W power amplifier drove the piezoelectric actuator. The QuickPack Power Amplifier controls QuickPack type actuators and other piezoelectric devices

through applied voltage. It accepts an input signal to provide an output of up to ±200 V at 200 mA with a bandwidth up to 7.5 kHz. The input range of the amplifier is 0 to ±10 V. The function generator used to send the signal to the actuator through the amplifier was from the Advanced LabVIEW 6.0, a graphical programming system that controlled data acquisition and analysis data, and the BNC-2090 from National Instruments. The program sent a 5-volt square wave to the QuickPack Power Amplifier. The period of the function was twice the desired actuation time.

The data acquisition card used was a National Instruments PCI-MIO-16E-4 card. It allows up to 16 analog inputs, two12-bit analog outputs, a 12-bit resolution, up to 500 kS/s sampling rate, eight digital input/output lines and a 24-bit counter. The BNC-2090 is a shielded, rack-mountable BNC adapter chassis. It consists of twenty-two BNC connectors for analog, digital, and timing signals, twenty-eight spring terminals for digital/timing signals, and finally, silk-screened component locations for passive signal conditioning. The LabVIEW program was used in conjunction with the data acquisition and analysis software for the constant temperature anemometer.

3.2. EXPERIMENTAL SET-UP

The aluminum flat plate was mounted in the test section of the wind tunnel. The rectangular shaped piezoelectric bimorph actuator was placed so that its trailing edge was 498.5 mm from the leading edge of the plate. The array of eight hot-wire sensors was located at two different positions. In the first position, the first row of sensors, those closest to the actuator was 3.0 mm downstream from the trailing edge of the actuator, or 501.5 mm from the leading edge of the plate. In the second position, it was

located 26.5 mm downstream of the actuator, or 525 mm from the leading edge. Testing at the two different locations allowed observation of the turbulent burst evolution in time and space. Natural bursts occur in a space 100-1000 wall units long, which is approximately 10-240 mm under the conditions in this work. However, since the bursts were artificially created, the sensors were arranged from approximately 10-320 wall units from the actuator in order to watch the evolution and to see the effects of the flap actuator in greater detail.

The eight hot-wire sensors were arranged in three rows, each row separated by 0.3 inches, shown in Figure 3.3. The first two rows had three sensors in each row. The distance from center to center of each probe was 0.2 inches. The third row consisted of two sensors, staggered in between the first two rows. These two sensors were also 0.2 inches apart, center-to-center.

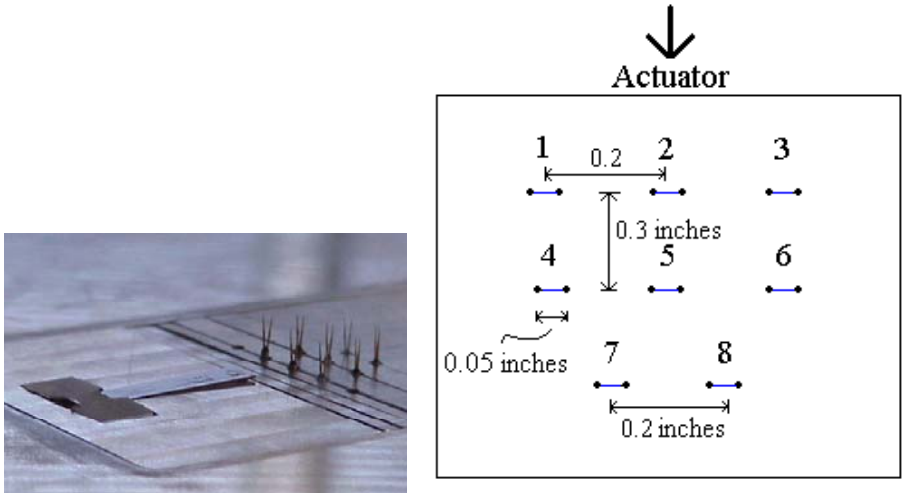

Figure 3.3. Probe Array and Actuator Set-up.

Two clamps supported the probes. The first clamp was the larger of the two clamps and was suspended underneath the plate by four rods and held the probe connectors in place.

The second clamp was mainly used for probe alignment and was built as a slot in the plate as shown in Figure 3.4.

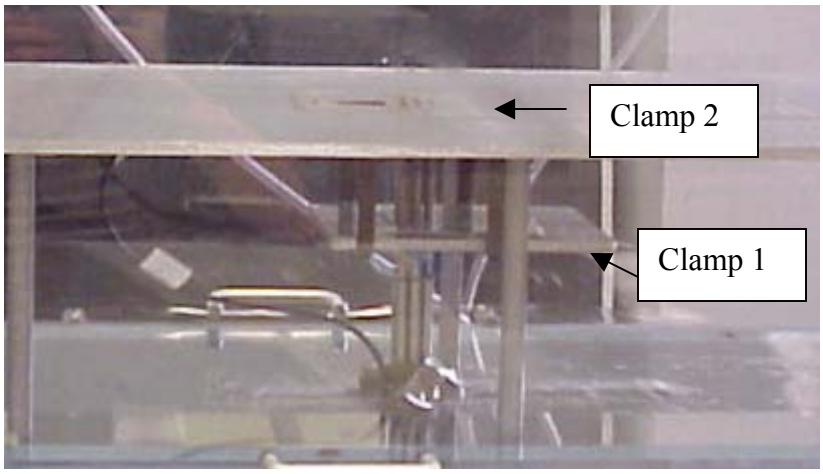

Figure 3.4. Probe Clamps.

The presence of the six legs of the plate, the large clamp, the probe supports and the probe cables, inhibits the flow from moving at the same speed underneath the plate as on top. Because of this, much of the flow was forced to the top of the plate at a positive angle of attack, α. Because this division of flow was uneven, separation occurred at the leading edge of the plate. To overcome this separation, two rows of 25 mm^2 small grate was placed at the trailing edge of the topside of the plate. The wire evened out the flow.

The tests were completed in a zero pressure gradient flow at four different freestream velocities, 0.5, 1.0, 1.5 and 2.0 m/s. In order to conduct experiments in a turbulent boundary layer, a boundary layer trip was used consisting of four three inch by 1 inch pieces of 220 grit sandpaper were staggered 0.5 inches from the leading edge.

From past studies, turbulent bursts have been best sensed at $y^+ = 15$. In this experiment, the location of the bursts correlates with the height of the actuator. The

displacement of the actuator was 0.7 mm (0.0275 inches), so the sensors took measurements at a range of heights, from 0.5 mm to 5.0 mm.

Table 3.3 shows velocity measurements taken at the various probe heights in the range of $5 \le y^+ \le 25$. Table 3.3 also includes various parameters for two distances from the leading edge to the middle row of sensors, 59 cm and 54 cm. The middle row of sensors in the array was chosen because the values for the first and third row of the sensors did not have much of a variance from the middle row of sensors. Table 3.3 gives the theoretical flow parameter values for if the thickness of the turbulent boundary layer were equivalent to that of the laminar boundary layers. Included values in the table are Reynolds numbers, Re_x, the theoretical laminar boundary layer height, δ_{lam}, the theoretical turbulent boundary layer height, δ_{Turb}, and the corresponding y values in laminar and then turbulent flow for $y^+ = 15$, for the two distances from the leading edge. Although the experiments were conducted in the laminar and transition regions, the calculations are made as if the flow were turbulent with to compare with previous data.

U (m/s)	Re_{1x}	Re_{2x}
0.5	18,206	19,294
1	36,412	35,589
1.5	54,619	57,881
2	72,825	77,179
U (m/s)	δ_{lam1}	δ_{lam2}
0.5	20 mm, 0.795 in	19.6 mm, 0.77 in
1	14 mm, 0.56 in	13.8 mm, 0.55 in
1.5	11 mm, 0.46 in	11 mm, 0.45 in
2	10 mm, 0.39 in	9.8 mm, 0.39 in
U (m/s)	δ_{Turb1}	δ_{Turb2}
0.5	27 mm, 1.08 in	28.6 mm, 1.13 in
1	23.8 mm, 0.94 in	24.9 mm, 0.98 in
1.5	21.9 mm, 0.87 in	23 mm, 0.91 in
2	20.7 mm, 0.82 in	21.7 mm, 0.86 in
U (m/s)	$y_{(y+=15)1}$	$y_{(y+=15)2}$
0.5	6.5 mm, 0.255 in	6.6 mm, 0.26 in
1	3.5 mm, 0.138 in	3.5 mm, 0.14 in
1.5	2.5 mm, 0.098	2.5 mm, 0.098
2	2 mm, 0.079 in	1.9 mm, 0.075

Table 3.3. Corresponding Testing Parameters.

Table 3.3 is referred to in the results section as a concise summary of test parameters.

4. RESULTS

A number of test runs were made to characterize the effect of flap actuation on the flow, within the turbulent boundary layer. The tests were conducted in a zero pressure gradient flow at four different freestream velocities, 0.5, 1.0, 1.5 and 2.0 m/s. In order to conduct experiments in a transition boundary layer, a boundary layer trip was used consisting of four three inch by 1 inch pieces of 220 grit sandpaper were staggered 0.5 inches from the leading edge. The actuator was set at a maximum displacement of 0.7 mm into the turbulent boundary layer. The sensors were placed at a height range of 0.5 mm to 5.0 mm from the flat plate into the boundary layer, and at two downstream distances from the piezoelectric actuator, 3.0 and 26.5 mm. These measurements are from the trailing edge of the actuator to the downstream location of the first row of probes in the array. The duration of activation included four values; 0.5, 0.25, 0.1 and 0.05 seconds. Table 3.3 shows flow characteristics for each different freestream velocity and distance.

A hot-wire probe was first used to obtain mean and rms streamwise velocity profiles for the laminar and tripped cases for two velocities, $U = 0.5\,\text{m/s}$ and $U = 2.0\,\text{m/s}$, shown in Figures 4.1 and 4.2 respectively. The measurements were made from $y = 0.0 - 20.0\,\text{mm}$, approximately, $0 \le y^+ \le 135$, at 0.5 m from the leading edge of the plate. Because the work was completed within the boundary layer and the probes were difficult to see and position accurately, a small variation in height could produce a large velocity difference when close to the wall. Figures 4.1.a and 4.2.a show the boundary layer profiles, Figures 4.1.b and 4.2.b show the rms velocities, Figures 4.1.c

and 4.2.c plot data against the Blasius curve, and Figures 4.1.d and 4.2.d plot data against turbulent curves.

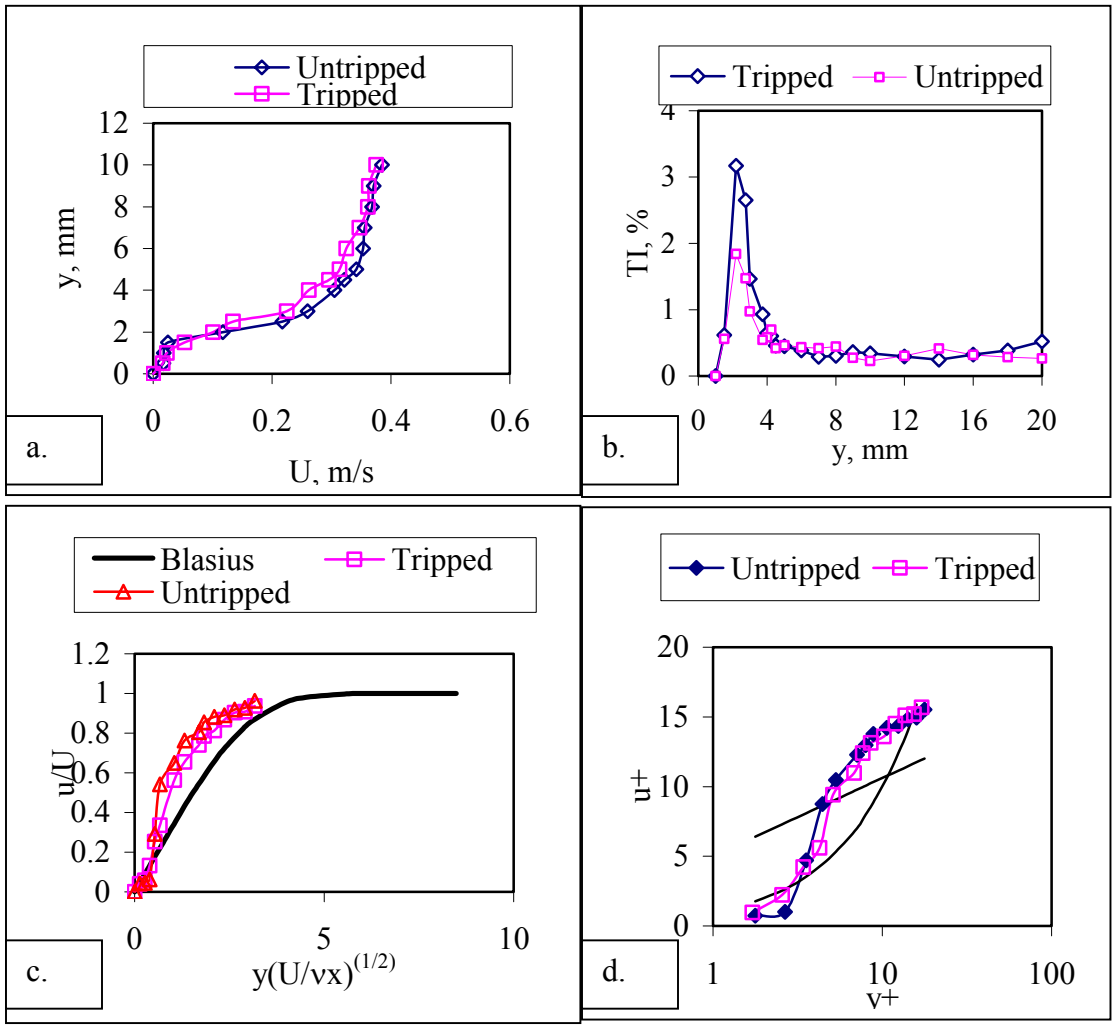

Figure 4.1. Boundary Layer Profiles and Turbulence Intensities for $U = 0.5$ m/s **(a)** Boundary Layer Profile **(b)** Turbulence Intensity **(c)** Blasius Profile **(d)** Law of the Wall.

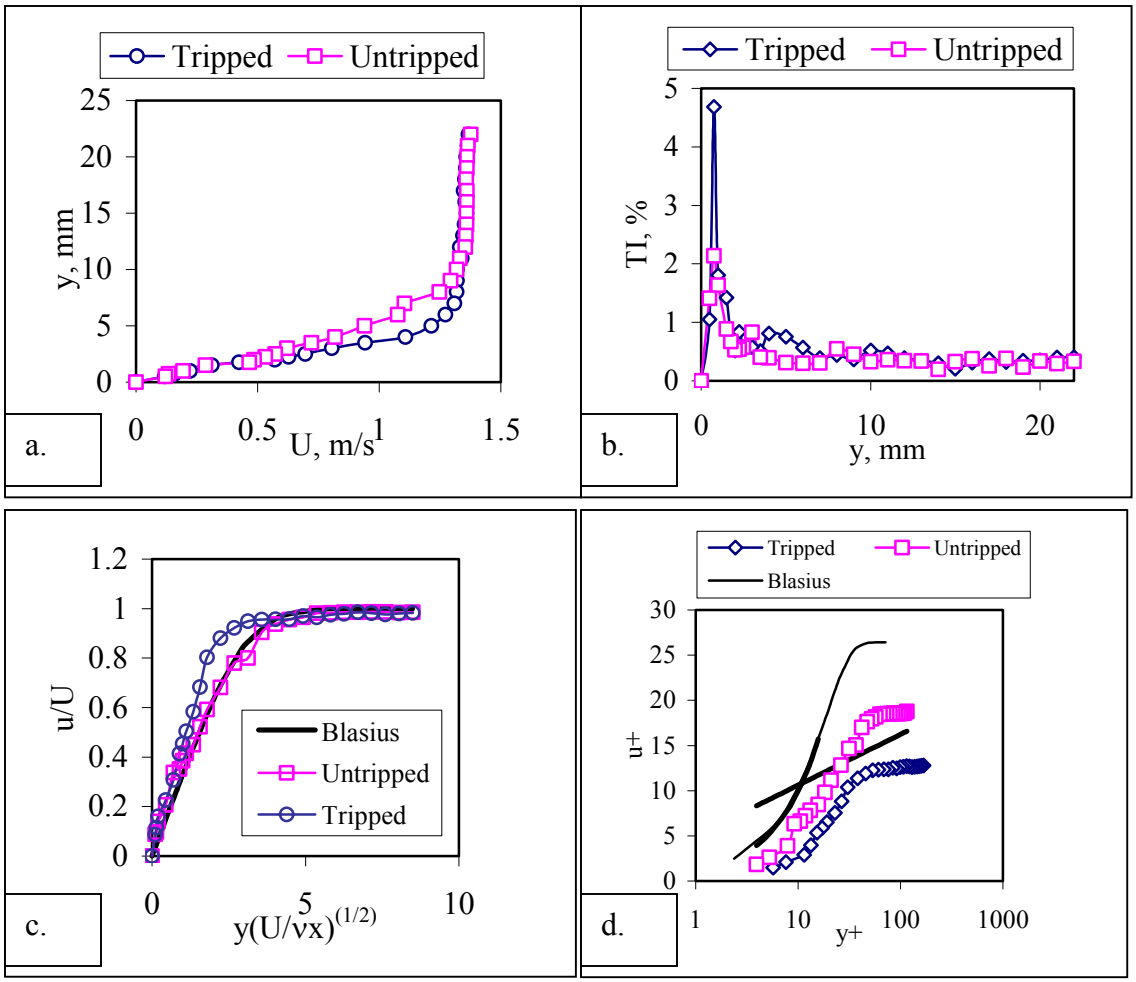

Figure 4.2. Boundary Layer Profiles and Turbulence Intensities for $U = 2.0$ m/s **(a)** Boundary Layer Profile **(b)** Turbulence Intensity **(c)** Blasius Profile **(d)** Law of the Wall.

The intent of the work was to compare the laminar and transition cases, which occured when the flow was tripped at the leading edge. To determine whether the flow was laminar or in the transition region, the data were plotted against the Blasius profile, defined for laminar boundary layers, and against the inner-law profile, defined for turbulent boundary layers. From Figures 4.1 and 4.2, it appears that neither the tripped

nor untripped cases produced fully turbulent boundary layer flow. When the freestream velocity was 0.5 m/s, the effect from the boundary layer trip was minimal, although the turbulence intensity in the tripped case appears greater than for the untripped flow. The theoretical Reynolds number at a freestream velocity 0.5 m/s was 18,206 and was not high enough to be tripped into the turbulent domain. When the freestream velocity was 2.0 m/s, the theoretical Reynolds number was 72,800, and when tripped, was forced into the transition region. Since the Reynolds numbers were too low for the flow to be forced completely into the turbulent domain, the experiments were conducted in the laminar and transition regions. Figure 4.2.c shows that the slope of the tripped plot is steeper than the Blasius plot due to a higher shear stress. A higher freestream velocity was not chosen because to the geometry of the coherent structures would have required a sensing array of substantially smaller dimensions. In the future microsensors and actuators could be used to study higher velocities, and thus, higher Reynolds numbers. Herein the calculations are made with respect to turbulent boundary layers to make comparable references to previous data.

For the most part, probes 2, 5, 7 and 8 experienced the ejection phase of the burst process. The outside probes in the first two rows, probes 1, 3, 4 and 6, primarily sensed flow "filling-in" the central flow deficit. Thus, it will be seen that the central probes showed reduced velocities caused by flap actuation while the outside probes showed increases.

Figure 4.3 shows that actuating the piezoelectric bimorph actuator causes a velocity defect, $U_{d,}$, of approximately 12%, based on local velocities to occur. This set of data was taken with probe 2 at $y^+ = 6$, $U_\infty = 1.0\,\text{m/s}$, at a 3.0 mm distance

downstream from the tip of the actuator. On de-actuation of the bimorph actuator, the deficit is eliminated but an overshoot of velocity compared to the mean velocity occurs. For both the tripped and untripped cases, the duration of the velocity deficit was 0.6 sec, one tenth of a second longer than the actuation time, T_a, and there was a propagation delay between actuation time and deficit. There is very little difference between data taken in the tripped and untripped flows, in the deficit or length of bursting process.

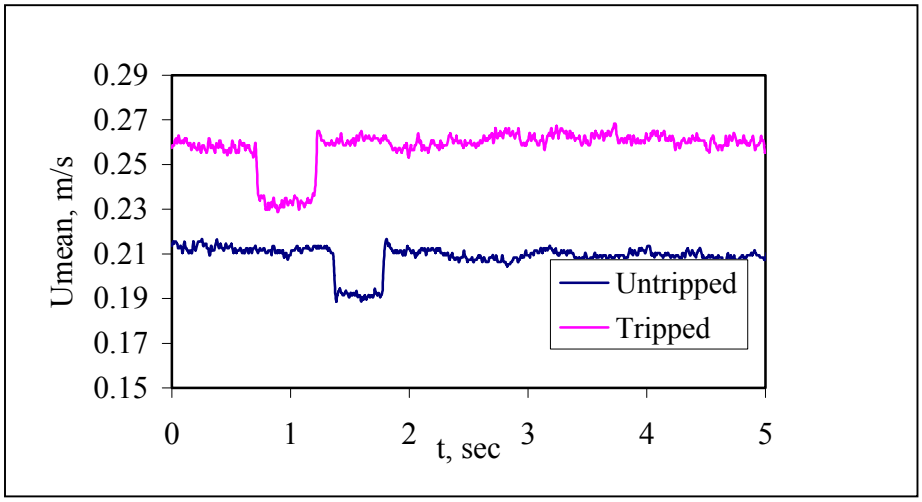

Figure 4.3. Tripped versus Untripped Data.

Data were taken at four different freestream velocities, 0.5 m/s, 1.0 m/s, 1.5 m/s, and 2.0 m/s. Figures 4.3 and 4.4 show the effect of the freestream velocity on the artificial bursting process for two cases. The length of time the actuator was energized was $T_a = 0.25$ seconds, and the probe was located at a height of 2.0 mm, for both cases. The data for the first case were taken 26.5 mm downstream from the actuator, while for the second case, it was 3.0 mm downstream from the actuator. In both cases, the velocity signal from probe 2 is shown. Probe 2 was the center probe of the first row.

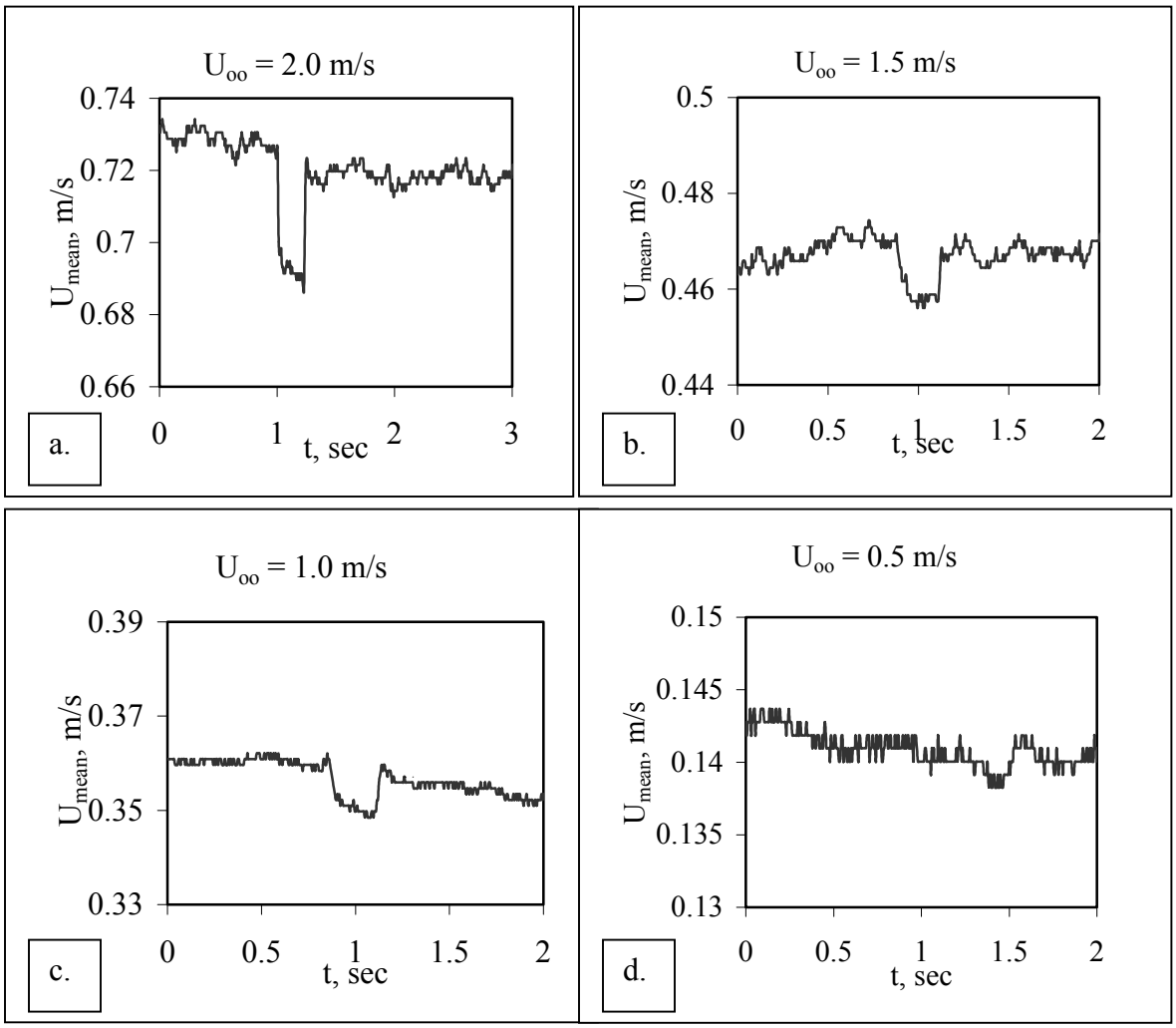

Figure 4.4. Raw Data Plots for Four Velocities taken with probe 2, $x = 26.5$ mm **(a)** $U_\infty = 2.0$ m/s **(b)** $U_\infty = 1.5$ m/s **(c)** $U_\infty = 1.0$ m/s **(d)** $U_\infty = 0.5$ m/s.

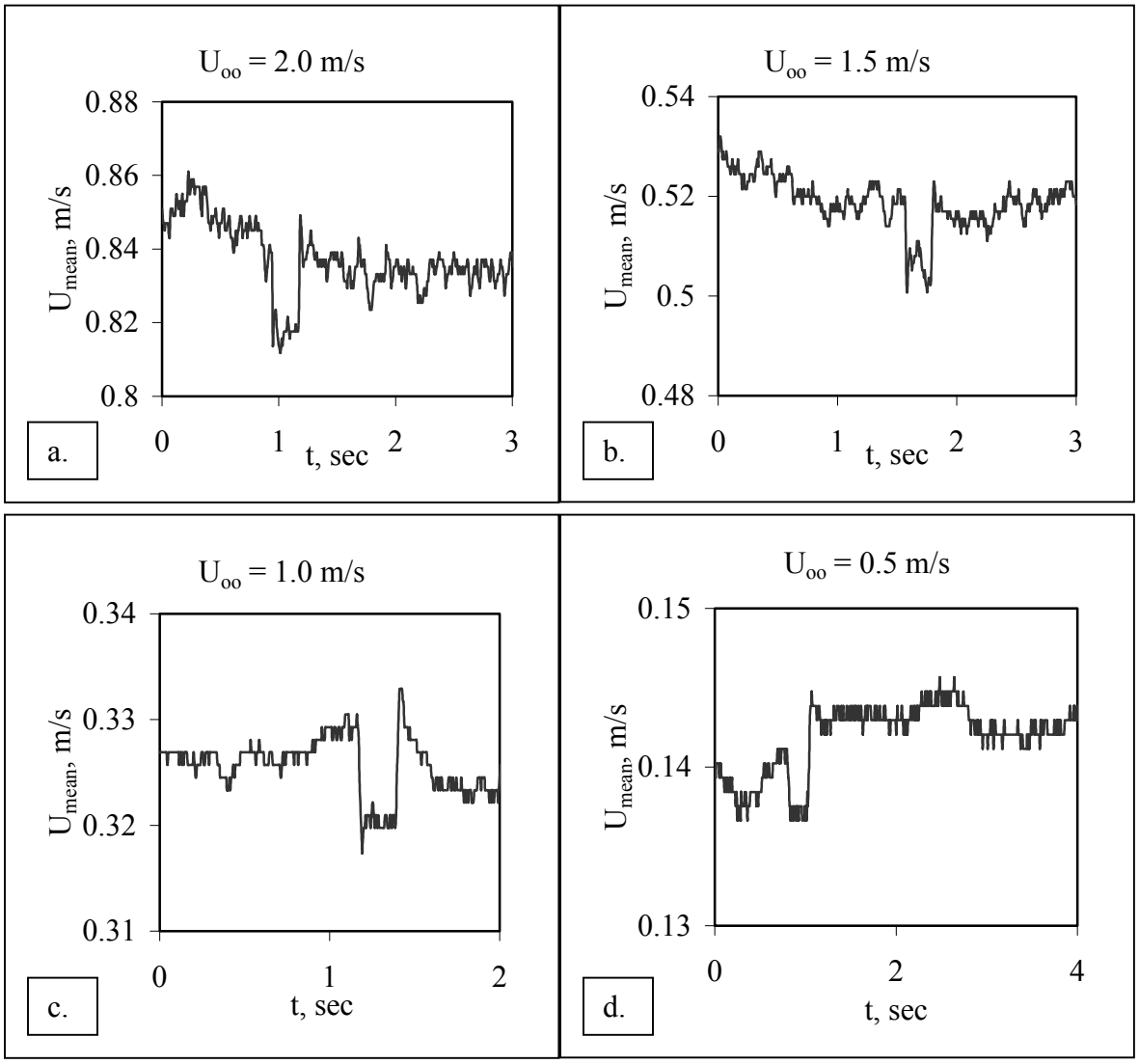

Figure 4.5. Raw Data Plots for Four Velocities, taken with probe 2 $x = 3.0\,\text{mm}$ **(a)** $U_\infty = 2.0\,\text{m/s}$ **(b)** $U_\infty = 1.5\,\text{m/s}$ **(c)** $U_\infty = 1.0\,\text{m/s}$ **(d)** $U_\infty = 0.5\,\text{m/s}$.

As can be seen in the Figures 4.4 and 4.5, and summarized in Figure 4.6.a, the percentage velocity defect, D_f, and free stream velocity are directly proportional; the velocity deficit caused by the actuator increases as the local velocity outside the boundary layer increases. The maximum velocity deficit is approximately 3.5% of the

freestream velocity, and the minimum, occurring at $U_\infty = 0.5$ m/s, is less than 0.5% of the freestream velocity for the range studied. The velocity seems to have no effect on the time required for the artificial burst cycle, T_b. This behavior is illustrated for both cases in Figure 4.6.b, where T_b is plotted as a function of freestream velocity for constant actuator deflection time of $T_a = 250$ ms. The downstream distance of the probe was 3.0 and 26.5 mm from the actuator.

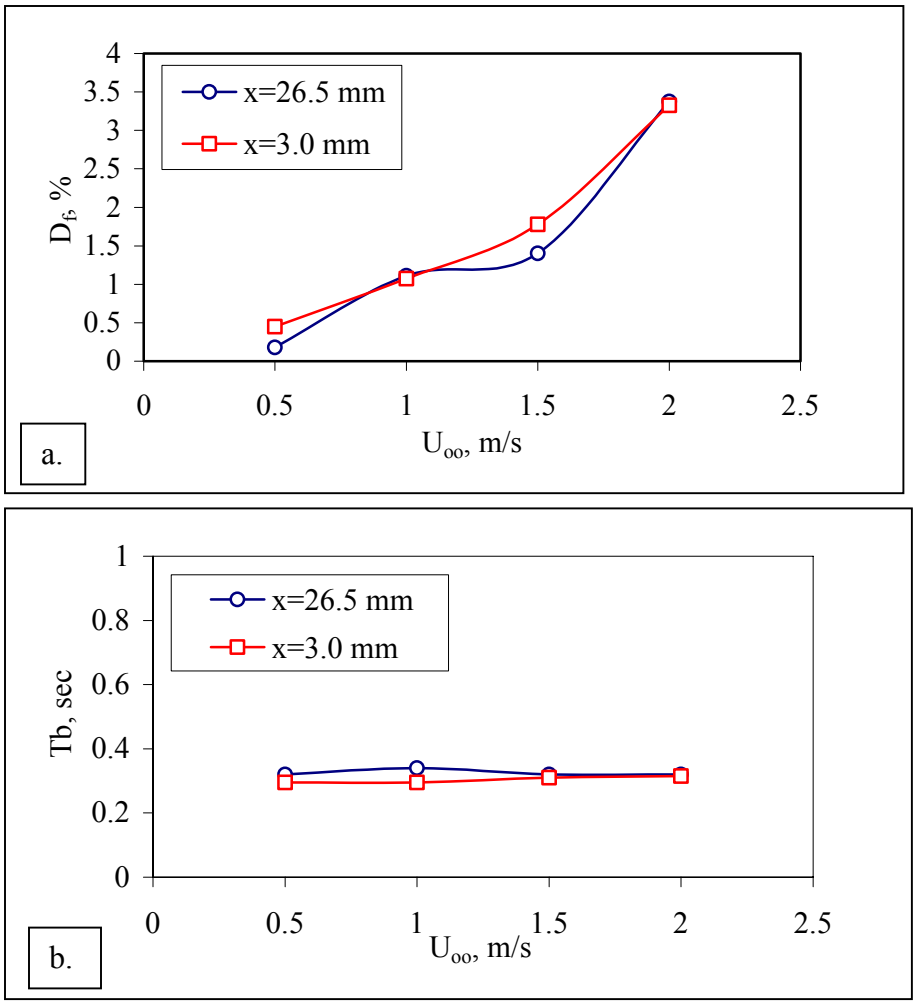

Figure 4.6. (a) Effect of Speed on Velocity Defect **(b)** Effect of Speed on Length of Burst.

Figure 4.7 shows the variation of the velocity defect of the artificially generated turbulent bursts as a function of distance from the wall, y. Three cases of data are shown. In the first case, Figure 4.7.a, the actuation time was 0.5 sec, the freestream velocity was 1.5 m/s, and the boundary layer thickness, δ, was 22.0 mm. In the second case, Figure 4.7.b, the actuation time was 0.05 sec, the freestream velocity was 1.0 m/s, and the boundary layer thickness was 23.8 mm. Both plots are normalized by the local velocity, U. Figures 4.7.a and 4.7.b show the velocity defect for four different heights, 5.0, 3.0, 1.0 and 0.5 mm. Both sets of data were taken using probe 2, which was located along the centerline of the actuator, 3.0 mm downstream from the trailing edge.

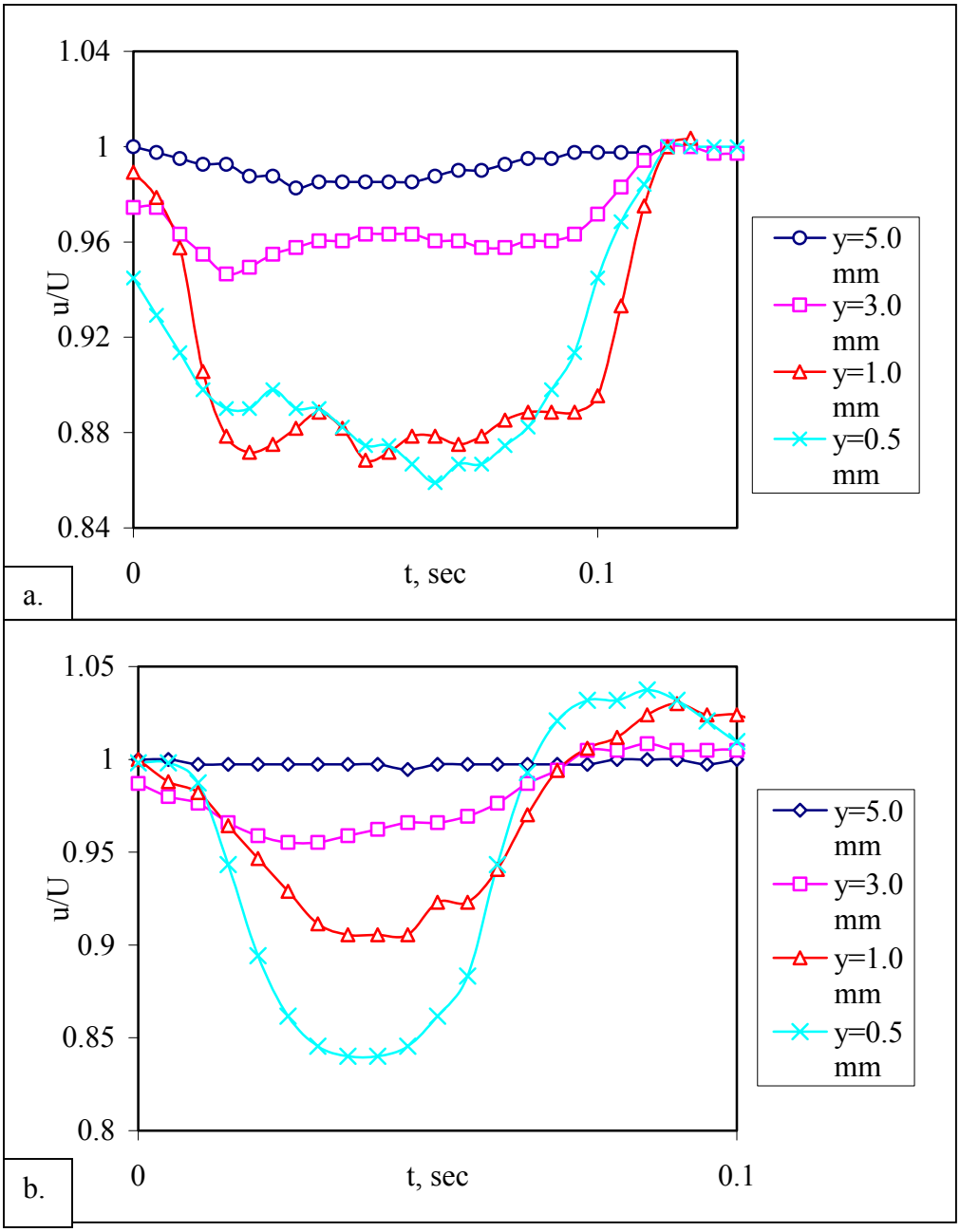

Figure 4.7. Velocity Defect at Four Different Heights, $x = 3.0$ mm **(a)** $U_\infty = 1.5$ m/s, $T_a = 0.5$ sec **(b)** $U_\infty = 1.0$ m/s, $T_a = 0.05$ sec.

Figure 4.7 shows that the relative velocity defect decreases as the distance from the wall increases for the range of measurements. There are two main differences between Figures 4.7.a and 4.7.b. In Figure 4.7.a, the velocity deficit reaches its maximum and levels off until the actuator is at rest, however, in Figure 4.7.b, the defect doesn't seem to level out in this way. The second difference is in Figure 4.7.b, where the plot shows a large velocity overshoot that is not evident in Figure 4.7.a. This overshoot is due to the de-actuation of the flap, and weakens as the distance from the wall increases. This overshoot represents the closing of the rectangular vortex filament as explained in the next section. Since the freestream velocity is faster in Figure 4.7.a, its magnitude dominates, and the overshoot seems smaller. Alternatively, this may be a reaction of the flow with the wall; momentum is reflected back into the outer flow as hypothesized by Ho *et al.,* when pitching a MEMS device into the flow.

Figure 4.8 shows the sequence of events leading to the artificial bursts; the effect of fluid withdrawal in the boundary layer due to the ejection of near wall fluid. The probe was located 3.0 mm from the actuator, the actuation time was 0.25 sec and the freestream velocity was 2.0 m/s. The theoretical boundary layer thickness, δ, was 20.7 mm. Figure 3.7.a shows five mean velocity profiles during a burst. At $t = 0.0$ sec, the actuator is at rest. At $t = 0.02$, 0.1 and 0.2 sec, the burst is evolving. At $t = 0.25$, the burst is complete. Figure 4.8.b shows an enlargement of the profiles, at time $t = 0.0$ and 0.1 sec wherein the defect is more apparent.

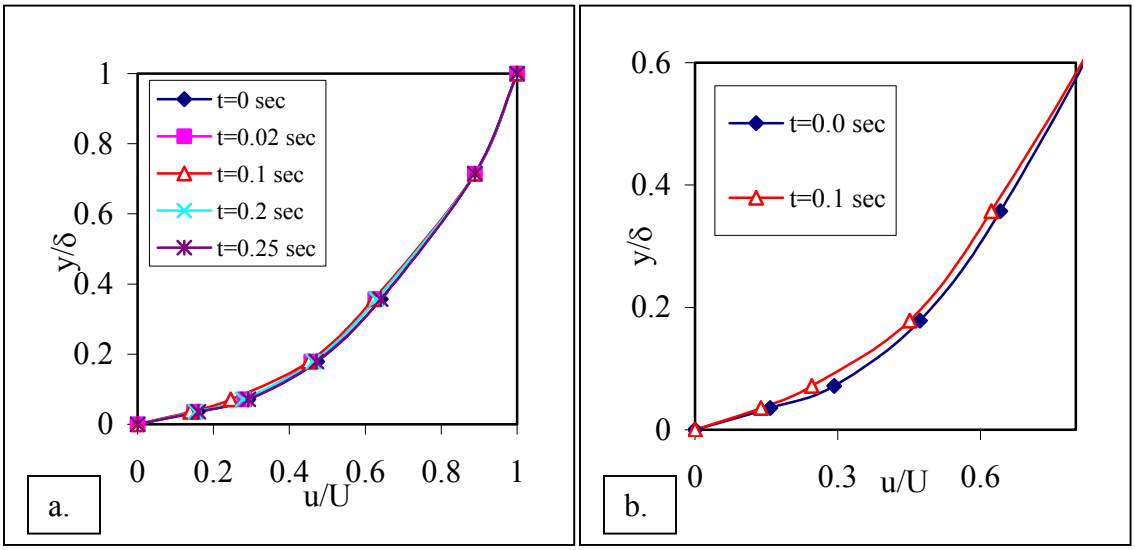

Figure 4.8. (a) Boundary Layer Velocity Deficit **(b)** Close-Up.

Figure 4.8 represents the tendency for inflexional velocity profiles to form during a burst. Such velocity profiles are dynamically unstable and eventually break down into a completely random pattern, as occurs in a burst. The inflections shown here are not as large as the visualization data of naturally occurring turbulent bursts studied by Gad-el-Hak and Hussain in 1986, but are very similar to the early stages of the formation of inflections. Visualization of the flap actuation, using a smoke wire, may show an inflexional velocity more analogous to those of Gad-el-Hak and Hussain.

Figure 4.9 shows the velocity defect versus time when the probe was located 26.5 mm downstream of the actuator and at two different heights, 2.0 and 3.0 mm. The actuation time was 0.25 sec, the freestream velocity was 1.0 m/s and the boundary layer thickness was 25.0 mm.

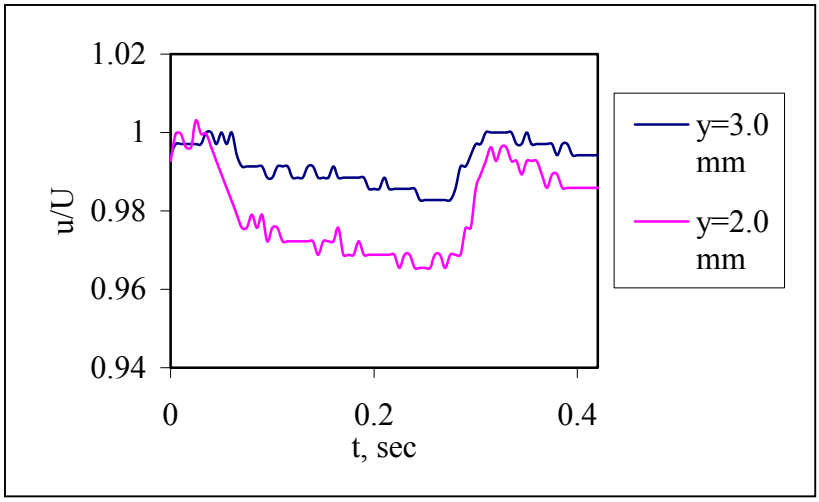

Figure 4.9. Velocity Defect at Two Different Heights, 26.5 mm From the Actuator.

The velocity seems to reach a maximum defect and level off, as it did in Figure 4.8.a. It does show a small overshoot, but its magnitude is not as large as in Figure 4.8.b.

Figure 4.10 shows how the defect varies with distance from the wall for all three cases shown above.

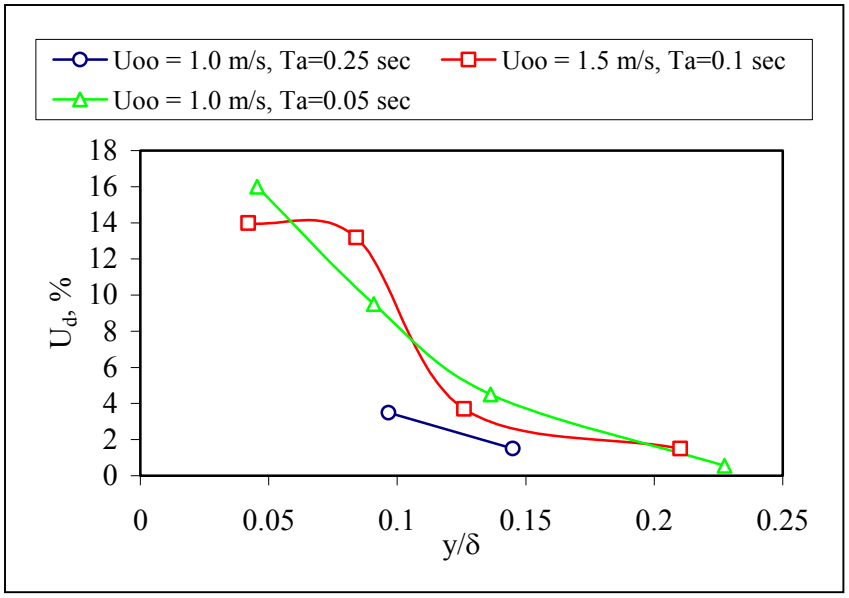

Figure 4.10. Effect of Height on Percent Defect.

The percent defect decreases as y/δ increases. The effect decreases because the actuator's deflection was 0.7 mm, so that most of the defect occurred at about this location. As the magnitude of the freestream velocity grew stronger, the strength of the effect diminished.

Figures 4.11 and 4.12 show the velocity defect as the burst propagated downstream. The distance of the probes downstream from the actuator varied, but the height of the probes remained constant. The probes were located along the centerline of the actuator at four distances: 3.0, 10.6, 26.5 and 34.0 mm. In Figure 4.11, the data were taken at a freestream velocity of 1.0 m/s, an actuation time of 0.10 sec, and a probe height of 3.0 mm. In Figure 4.12, the freestream velocity was 2.0 m/s, the actuation time was 0.05 sec, and the probes were located at a height of 2.0 mm. For Figures 4.11 and 4.12, (b), (c) and (d) are percent defect versus distance, plots of bursting time versus actuation time and bursting time versus downstream distance, respectively.

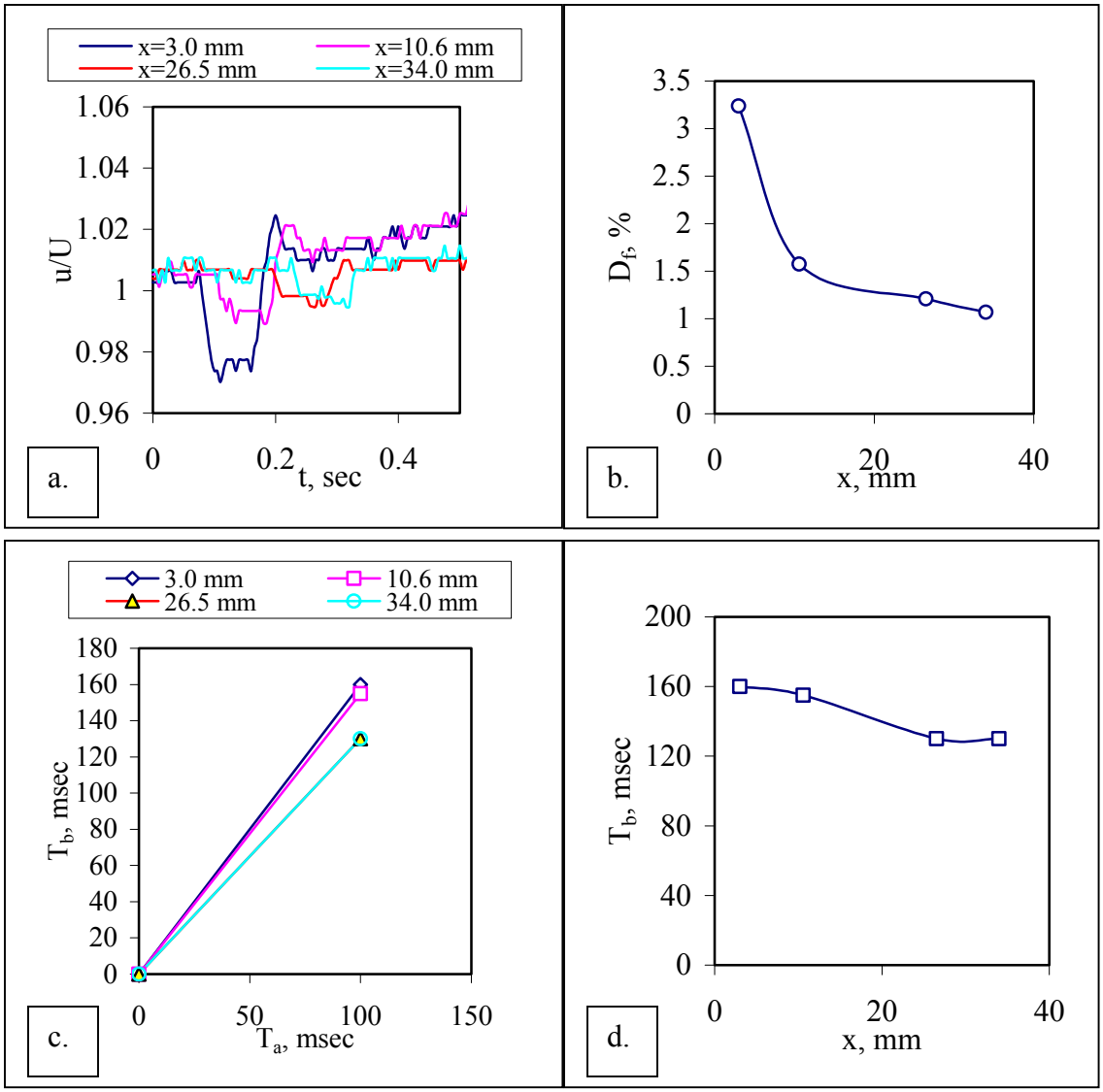

Figure 4.11. (a) Defect in Time, $U_\infty = 1.0$ m/s, $T_a = 0.1$sec, and $y = 3.0$ mm **(b)** Percent Defect versus Downstream Distance **(c)** Bursting time versus Actuation Time **(d)** Bursting Time versus Downstream Distance.

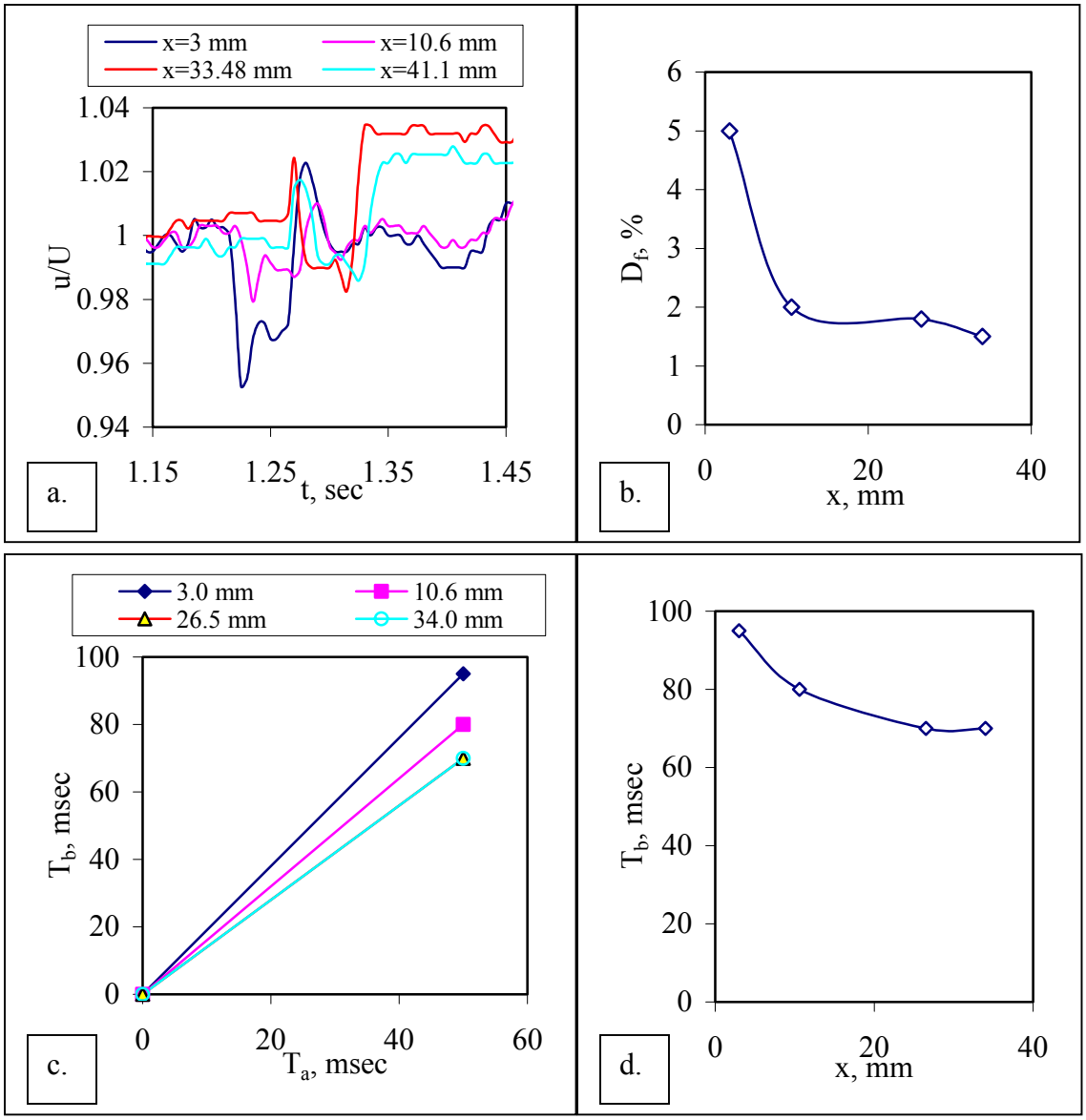

Figure 4.12. (a) Defect in Time, $U_\infty = 2.0$ m/sec, $T_a = 0.05$ sec, and $y = 2.0$ mm **(b)** Percent Defect versus Downstream Distance **(c)** Bursting time versus Actuation Time **(d)** Bursting Time versus Downstream Distance.

The bursting time, T_b, is defined as the time it takes for the flow to return to normal after it has been altered by the activation of the actuator. It is somewhat a subjective

measure in as much as some judgment is necessary to determine the time needed to recover "normality." The principal ambiguity has to do with the overshoot at the end of the event. When the overshoot is stronger, the duration appears longer.

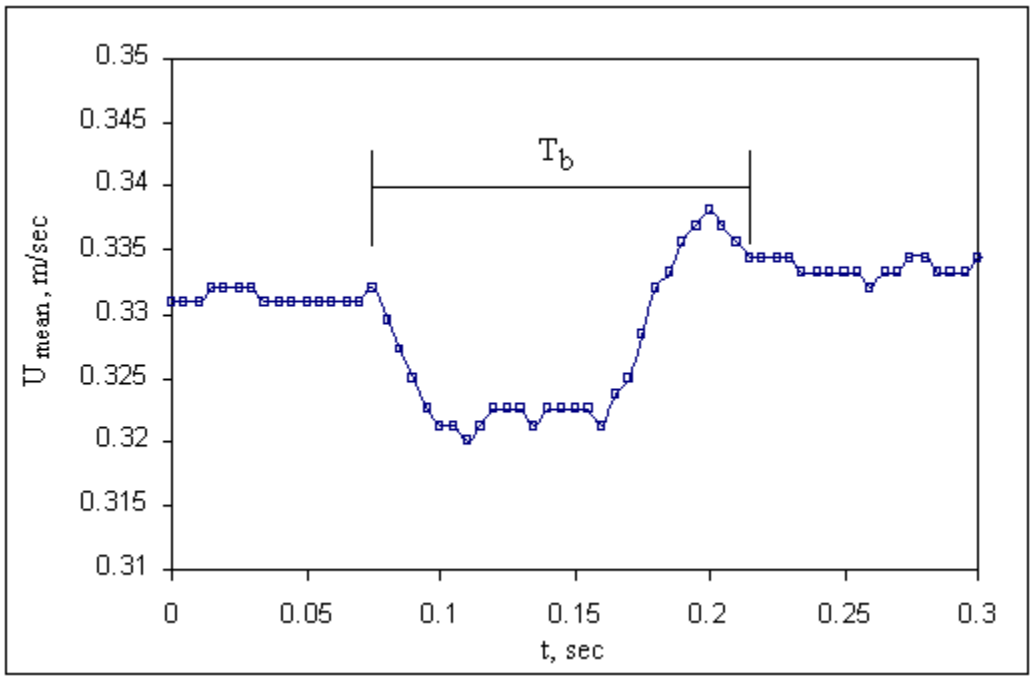

Figure 4.13. Definition of T_b.

In both Figures 4.11 and 4.12, the duration of the defect is longer that the length of time during which the actuator is activated. As the downstream distance from the actuator increases, the length of the defect diminishes, but still remains longer than actuation time. The velocity defect also decreases as the downstream distance increases. The largest difference in velocity defect appears to occur in the first few millimeters from the actuator. After 10.0 mm, the decrease is only slight.

Figure 4.14 shows the effect of four different actuation times, T_a, that were employed, 0.5, 0.25, 0.10 and 0.05 sec. In Figure 4.14.a, the freestream velocity was

1.0 m/s and the probe was located at a height of 2 mm, $y^+ = 8.5$, and at a downstream distance of 26.5 mm. In Figure 4.14.b, the freestream velocity was 2.0 m/s, the probe was located at a height of 1 mm, $y^+ = 8$, and at a downstream distance of 3.0 mm. As power was supplied to the actuator, it can be seen that the probes showed a slight increase in velocity, because during the time the actuator was moving from rest to actuation position, the defect grew. While the actuator was held in fixed displacement, there was a fixed velocity deficit, during which the slow moving fluid was being ejected from the wall to the outer flow. When the actuator returned to the rest position, which was flush to the wall, there was a fast increase in velocity rising a bit higher than the mean velocity, and then quickly returning to the mean flow value. The same behavior seems to happen for each actuation speed.

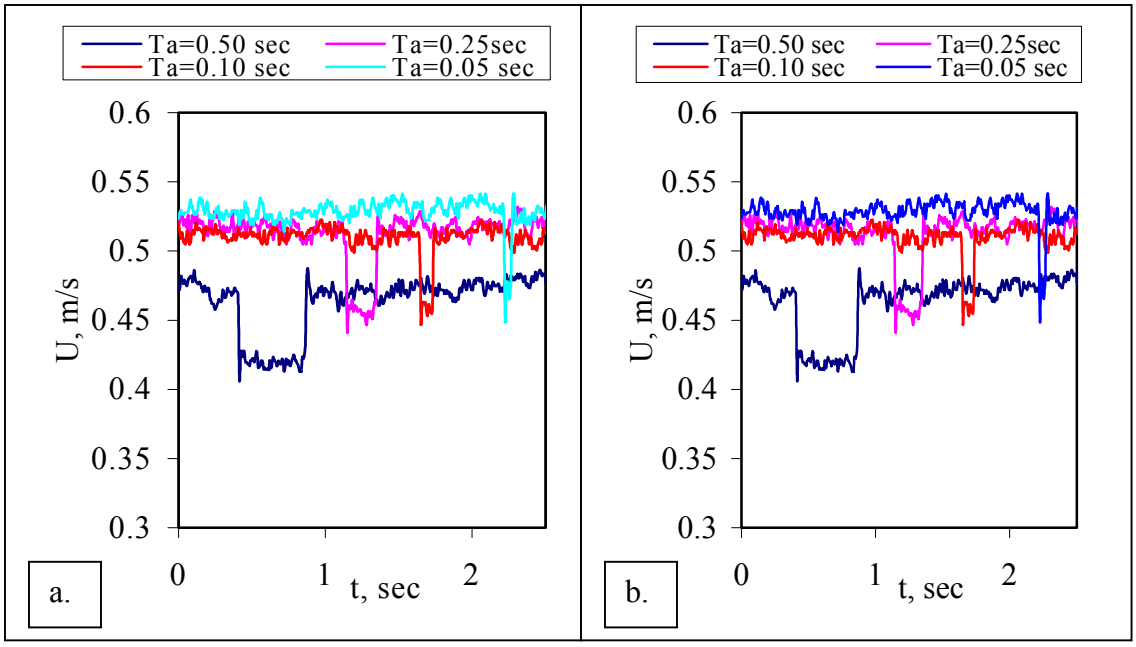

Figure 4.14. Velocity at Four Different Actuation Times **(a)** $U_\infty = 1.0$ m/s, $x = 26.5$ mm, $y = 2.0$ mm **(b)** $U_\infty = 2.0$ m/s, $x = 3.0$ mm, $y = 1.0$ mm.

Figures 4.15.a and 4.15.b compare the duration of the bursts with the duration of the actuation for the cases shown in Figures 4.14.a and 4.14.b respectively. It shows that the duration of the defect is longer that the length of time during which the actuator is activated. As the actuation time decreases, the bursting time shows a small increase.

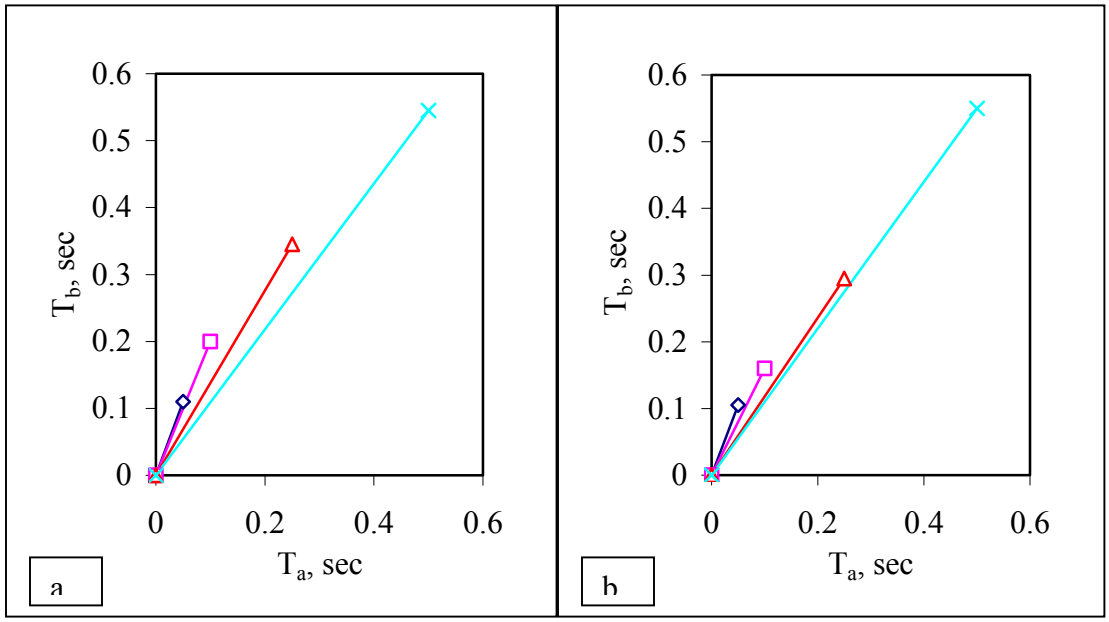

Figure 4.15. Comparison of T_a and T_b **(a)** $U_\infty = 1.0$ m/s, $x = 26.5$ mm, $y = 2.0$ mm **(b)** $U_\infty = 2.0$ m/s, $x = 3.0$ mm, $y = 1.0$ mm.

Past studies indicated that the bursting process lasts about 15 wall units, which in this work is equivalent to 20-50 msec. Due to the software limitations, the actuation time was limited to greater than 50 msec. However, when comparing previous work by Myose and Blackwelder, Kaplan and Blackwelder, and Gad-el-Hak and Hussain in 1986, our artificially generated bursts compare well with their data. Figure 4.16 compares artificial and natural bursts, from Gad-el-Hak and Hussain with the data from

this work. The American Institute of Physics granted permission for the use of the figure. The low speed streaks are represented by the dark blocks along the x-axis, and occur between the counter-rotating vortices. The measurements shown in Figure 4.16.b were completed at a freestream velocity of 1.5 m/s, at a height of 0.5 mm ($y^+ = 4$), and a distance downstream of the actuator of 3.0 mm.

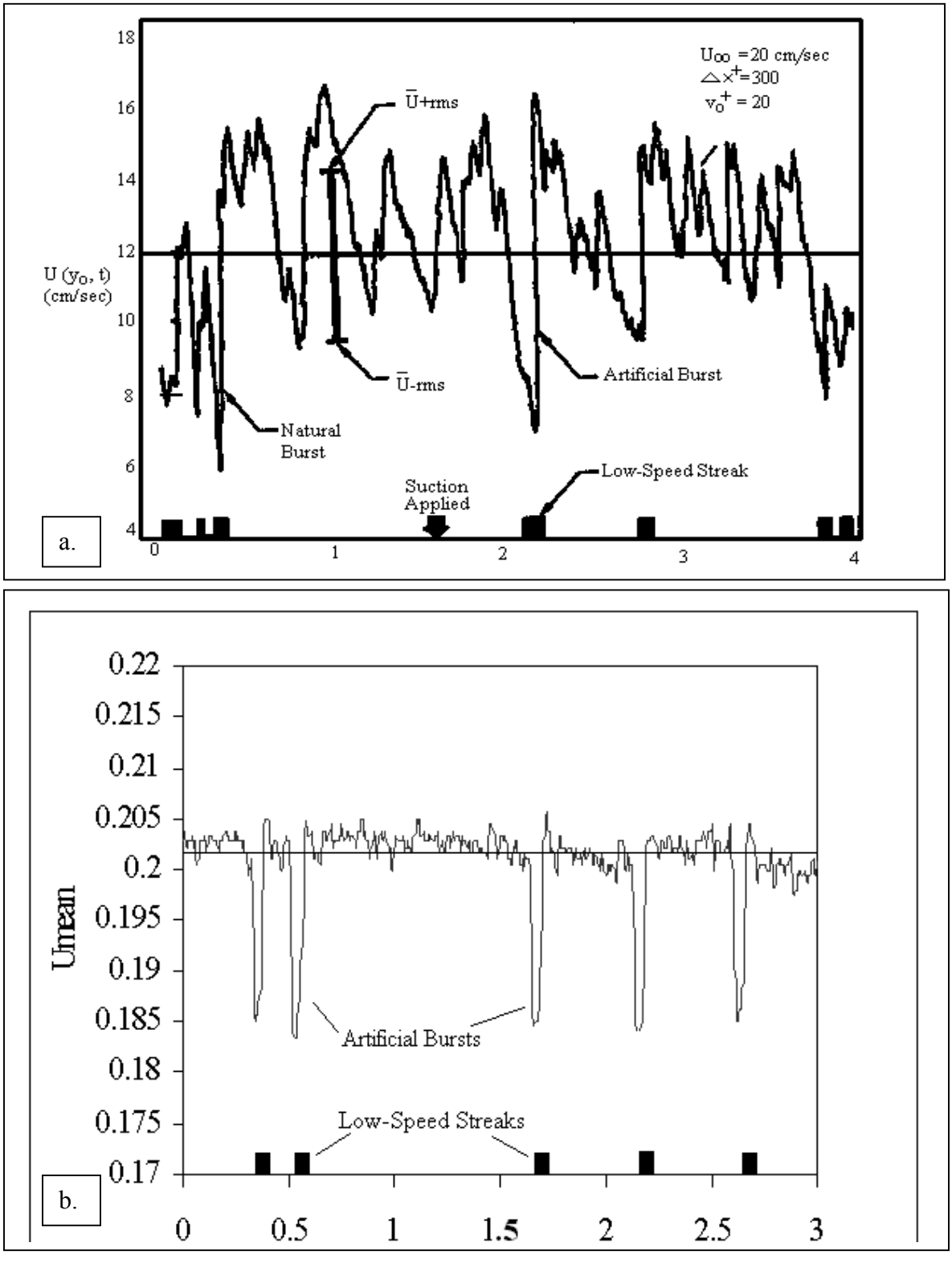

Figure 4.16. (a) Artificial and Natural Bursts (Gad-el-Hak, Hussain, 1986) **(b)** Artificial Burst from this Study.

In Figure 4.16.b, the actuator was activated five times at $T_a = 50$ msec. Both the data from this work and the data from Gad-el-Hak and Hussain [17] show a negative spike in the velocity data. The rapid acceleration linked with bursts are preceded by a low-speed streak. Due to the quickness of the actuation time, 50 msec, there is no time for the velocity defect to reach its maximum and remain fixed until the actuation returns to rest. In both Figures 4.16.a and 4.16.b, with every burst, naturally and artificially generated, there seems to be an overshoot of velocity after the rapid increase of velocity. The velocity defect of the artificially generated burst, in Figure 4.16.a, is approximately 45% and occurs in a turbulent flow, while the defect in figure 4.16.b is 10% and occurs in a laminar flow. The difference in percent defect between this work and the work of Gad-el-Hak and Hussain may be due to the variation of the flow as well as the magnitude of the piezoelectric actuator displacement, in this work.

The features of the artificial bursts may not be identical to those of natural bursts because of the variability in the initiation point, spanwise location and strength of the structures. The location of the hot-wire probes may not obtain data from the same section of the burst. Figure 4.17 shows this variation because probe numbers seven and eight obtained data from a different portion of the coherent structures.

Probe numbers 7 and 8 were located downstream of the actuator along the outer edge, as seen in Figure 3.3. Figure 4.17 shows that while probes 2 and 5 are located along the centerline of the actuator and obtain a decrease in velocity when the actuator was activated, probes 7 and 8 show an increase in velocity. The parameters of the flow were as follows: $U_\infty = 2.0$ m/s, $y = 0.5$ ($y^+ = 8$), $T_a = 0.1$ sec.

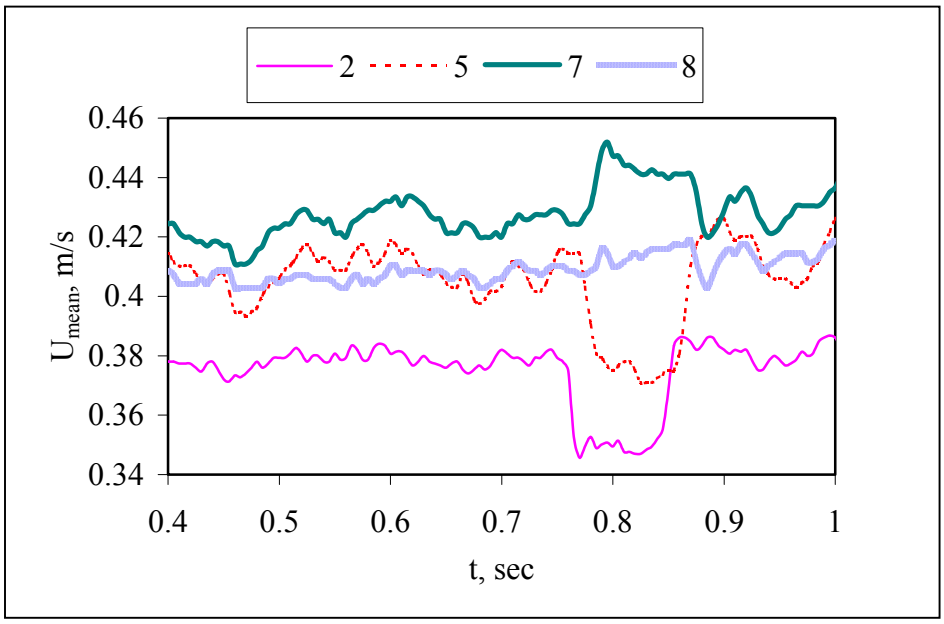

Figure 4.17. Mean Velocities of the Downwash and Upwash of the Vortices.

This increase in velocity is most likely due to the flow from the outer boundary layer being brought down towards the wall by the counter-rotating vortices produced by the actuation. Since the actuation time was so long, the velocities reached their maximum strength and remained fixed until the flap returned to rest. There is a time delay that depends on the distance between the probe and the burst generator. The increase in velocity agrees with data found by Gad-el-Hak and Hussain [17] of a natural burst, in which the probe saw a positive velocity spike as the burst passed over.

One way to understand the effect of the actuator on the flow is to imagine two longitudinal traveling vortices that eject fluid between then and entrain fluid from the

outside. The next section characterizes the effect of the piezoelectric actuator, followed by some conclusions and ideas for future work.

5. DISCUSSION

We have seen that using a flap actuator creates low-speed streaks, as are associated with the bursting process in laminar, transition and turbulent regions. Investigators have been studying methods of controlling the flow to prevent bursts, including the use of flap actuators. The present work concludes that the use of rectangular flap actuators, in fact, creates a burst-like flow field qualitatively similar to that found by Gad-el-Hak and Hussain. Figure 4.1 shows a conceptual model of the events that occur when the flap is actuated.

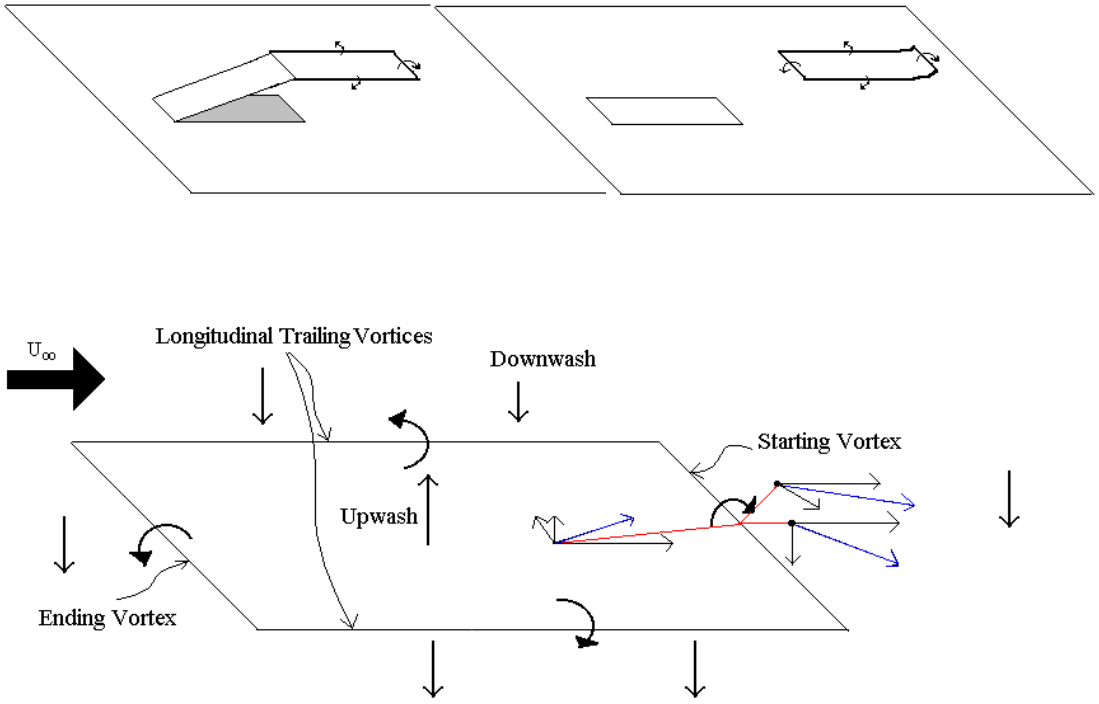

Figure 5.1. Vortex Filament Model.

The conceptual model derived in this work involves the creation of a starting vortex filament from the actuator. This vortex is analogous to the starting vortex associated with wing theory. Once the actuator is displaced, an open-ended rectangular vortex filament is created; the starting vortex plus two longitudinal trailing vortices. The hot-wire probes see the initial effect of the first vortex, but while the actuator remains in the displaced position, the probes see the effect of the two streamwise vortices. These streamwise vortices pull low velocity fluid from the near wall region towards the outer flow. Since the velocity of the flow closer to the wall is less than in the freestream, the hot-wire probes located along the centerline of the actuator see the lower velocity, or defect. When the flap actuator returns to rest, the vortex filament closes with an ending vortex so that a rectangular vortex filament structure remains. As the ending vortex passes a probe, an increase in velocity is seen, momentarily. The hot-wire probes see the effect of this rectangular structure as it convects downstream. The actual effect of the starting and ending vortices are small portions of the duration of the process, and therefore, the probes do not see their effect for very long. The closing vortex filament is believed to act as the high speed sweep occurring at the end of the bursting process. It brings higher moving fluid from the outer flow, back in to wash away the velocity defect. Finally the flow returns to normal. As the entire rectangular vortex filament moves downstream, it slowly moves upward, out into higher moving fluid, because the counter-rotating vortices are inducing upwards velocities on themselves. In this layout, the starting vortex is the first portion of the rectangle to move out into faster moving boundary layer fluid. The interior of the rectangle experiences upwash while the exterior experiences downwash.

6. CONCLUSIONS

A flap actuator is a good method to simulate the bursting process. The flap of the actuator creates a rectangular vortex filament, similar to both the horseshoe vortex hypothesis and the counter-rotating vortices hypothesis. The vortex filament is created instantaneously, as the flap is activated, and is closed after the flap returns to the resting position, creating a vortex in the opposite direction of the first one. Some past studies have seen both a decrease and an increase in velocity associated with bursts. However, studies observed the naturally occurring bursting processes, where the location of the probes is not always consistent with the location of the bursts. The decrease in velocity that probes 2 and 5 observed was that of the low-speed streaks occurring in between the two counter-rotating vortices. The fast increase and the overshoot can be correlated to the burst. The increase in velocity that probes 7 and 8 observed was the high-speed fluid being brought on the outer side of the streak due to the opposite rotation of the longitudinal vortices.

The effect of the simulated burst is confined to a certain region in the boundary layer due to the geometry and deflection of the piezoelectric flap actuator. Other investigators have concluded that natural bursts occur in regions analogous to that region studied in this work. In natural bursts, the best location to place a probe is a $y^+ = 15$, however the best location to place a probe with artificially generated bursts varies with the deflection of the actuator. If a different actuator with a different

geometry and deflection were used, then the effects might occur in a different region of the boundary layer.

There are three steps to systematically study artificial generation of turbulent bursts. Creating bursts in laminar boundary layers, where the flow is even and the boundary layer is thick, in the transition region, where bursting occurs intermittently and the boundary layer height is still fairly large, and in turbulent flows, where the boundary layer thickness is thin and bursting occurs more often. In this work, the velocities were limited to the laminar region, and in some cases the transition region, due to the desired size and geometry of the actuator, sensors, and generated coherent structures. The effects of the macro flap actuator are conceptualized in this work, and can later be applied to faster and more turbulent velocities and smaller sensors.

Due to the experimental set-up and the type of sensors used to gather data, it was difficult to obtain data in the lower region of the boundary layer. In the future, flush mount shear stress probes could be used to get the near wall data that the hot-wire probes could not obtain. There were small spaces in the clamps beneath the hot-wires that may have disturbed the flow, near the wall region.

From the data, it has been seen that as the freestream velocity increases, the percent deficit also increases, but the duration of the burst remains the same. As the distance from the flat plate increases, the velocity defect from the actuator decreases. This is true because the effect from the actuator decreases, while the magnitude of the freestream velocity increases, overruling the velocity defect magnitude. The maximum defect at a height of 0.5 mm from the wall was 16%. This decreased to less than 1% at a height of 5.0 mm from the flat plate.

From the data, as the downstream distance from the actuator increases, the velocity defect during the burst decreases. The largest decrease is over the first few centimeters. At 3.0 mm downstream of the actuator, the defect was around 3-5 %, while at 34 mm from the actuator, the defect was approximately 1 %. This makes sense because as the rectangular vortex filament moves downstream there could be a lift up of the filament and the magnitude of the freestream velocity dominates. Also, as the downstream distance from the actuator increases, time it takes for the bursting process to be completed decreases. At this time, this phenomenon remains unexplained.

Four different actuation times utilized, 0.5, 0.25, 0.1 and 0.05 sec. In the cases where the actuation time was 0.5, 0.25 and 0.1 sec, the velocity defect reached a minimum and remained fixed until the flap returned to rest. In naturally occurring turbulent bursts, the time it takes for the process to complete itself is approximately 15 wall units, 20-50 msec in these experiments. Due to software limitations, the fastest actuation time was 50 msec. However, when compared with data from other studies, 50 msec seemed to match very well.

Overall, using a rectangular piezoelectric flap actuator is an adequate method to create artificial turbulent bursts in a laminar boundary layer. In the past it has been tried to prevent the bursting process from occurring and therefore to reduce drag. However, as we know from observing the effects of pitching the actuator into the flow, a complicated burst-like process occurs. The next section gives ideas for future study of artificial generation and control of the turbulent bursting process.

7. FUTURE WORK

In this work, the experimental procedure was effective for observing the effects of the flap actuator. However, it only followed the bursting process from 0-300 wall units down stream of the actuator. In the future, perhaps a different wind tunnel with a longer test section could be used to obtain data from 0-1000 wall units downstream of the burst generator. Of course, there is a trade off between creating large enough structures for case of observation (i.e. thick boundary layers) and speed of event transpiration.

Past studies used primarily visualization techniques. In order to better compare current data with past data, visualization techniques, such as a smoke wire could be used in future study. Boundary layer instabilities were shown from hot-wire measurements but comparing these with photographs, may prove helpful.

In the near wall region, where it was difficult to place the probes, flushmount shear stress sensors may be used. This would help observe the effects of the pitching of the actuator into the flow. The hot-wire probes were able to be useful approximately 0.5 mm from the surface, but with flushmount probes, the data obtained will be even closer to the wall.

In the past, investigators have tried using flap actuators to control the bursting process, but due to the information gained in this work, we have seen that flap actuators can, in fact, simulate a turbulent burst. Future studies may bring answers to questions if the flap actuator would work to disturb the flow in order to prevent the high drag

inducing bursts, or would it in fact, increase the drag due to the creation of another burst type object. Lumley and Blossey found that by using a bump in the flow, which simulated a flap type movement, the drag was reduced on the order of 20%, however, the drag increased when the bump was lowered, which can be correlated to the sweep action of a burst. The location of the bump, or of a flap actuator is important. Perhaps if the flap were located between two low-speed streaks, the counter-rotating vortices would bring high-speed fluid down into the low-speed streaks. At the same time, on the outer side of the two streaks is high-speed fluid being brought down. This is the likely optimal location of the actuator. It would cause low speed fluid moving away from the wall to occur where this high-speed fluid was moving towards the wall thus counteracting the naturally occurring burst.

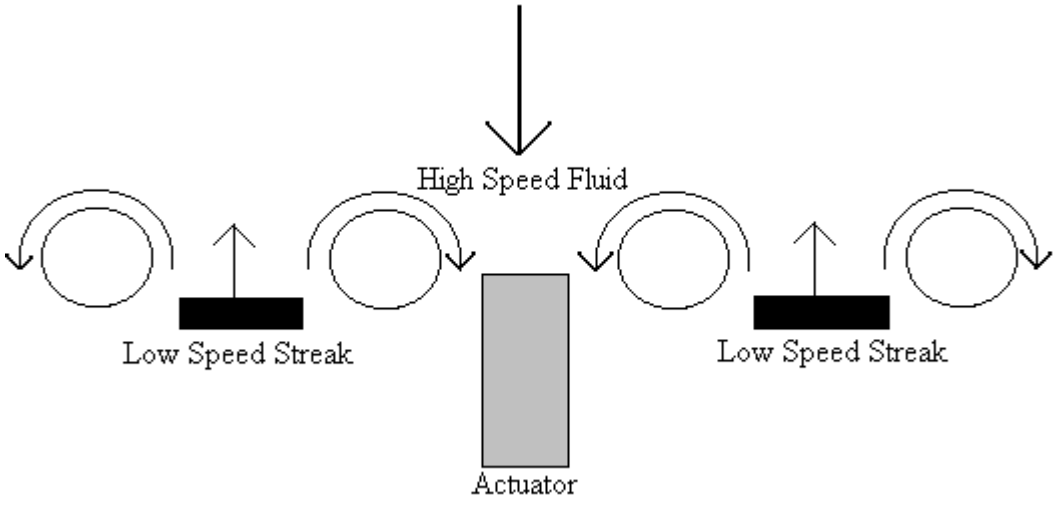

Figure 7.1. Proposed Location for Actuator for Control.

Delta wing shaped flappers and suction have been used in the past to generate artificial bursts. Perhaps in the future, other shapes and methods could be tried. Simple ideas such as uncovering slots in the plate could be tried. This may disrupt the flow

without creating low-speed streaks. However, it may cause higher drag because the higher moving flow would move down to fill in the space. We have seen that suction has successfully simulated a burst from Gad-el-Hak and Hussain [17]. The idea of blowing may be used to stop the bursts from occurring because it will stop the low speed streaks from occurring, by blowing a higher speed fluid into the lower speed streak region. However, some studies have shown that, while an event may reduce drag, completion if the device's cycle increases drag.

All of these ideas and the use of MEMS to place all sensors and actuators on one chip will allow a better study and resolution to the bursting process dilemma. MEMS will facilitate resolutions of relevant scales at high-Reynolds-number turbulent flows. Arrays of MEMS make it possible to obtain complete information of small-scale coherent structures. Wall shear and pressure sensors can be used to detect the beginning of the bursting process, and then the actuators can control it. MEMS, since they are smaller in size, will also be able to generate artificial bursts on a smaller level, more similar to what occurs naturally. The problem still arises about how to predict low-speed streaks before they occur, and not while they are occurring. Future study may help solve that problem.

8. REFERENCES

[1] Anderson John D. Jr. Fundamentals of Aerodynamics. McGraw-Hill, Inc., New York, 1991.

[2] Blackwelder R. F. and Eckelmann H. "Streamwise Vortices Associated with the Bursting Phenomenon," J. Fluid Mech. Vol. 94: 577-594, 1979.

[3] Blackwelder R. F. and Haritonidis J. H. "Scaling of the Bursting Frequency in Turbulent Boundary Layers," J. Fluid Mech. Vol. 132: 87-103, 1983.

[4] Blackwelder R. F. and Kaplan, R. E. Journal of Fluid Mech. Vol. 76: 89, 1976.

[5] Bradshaw P. "'Inactive Motion and Pressure Fluctuations in Turbulent Boundary Layers," J. Fluid Mech. Vol. 30: 241-258, 1967.

[6] Bushnell D. M. and McGinley C. B. "Turbulence Control In Wall Flows." Annual Review of Fluid Mechanics. Vol. 21: 1-20, 1989.

[7] Comte-Bellot Genevieve. "Hot-Wire Anemometry," Ecole Centrale de Lyon. 209-231, 1976.

[8] Coughlin K. and Marcus P. S. "Turbulent Bursts in Couette-Taylor Flow," Physical Review Letters, Vol. 77: 2214-2217, 1996.

[9] Dahm W. J. A. and Diez-Garias F. J., " Microactuator Arrays for Sublayer Control in Turbulent Boundary Layers Using the Electrokinetic Principle," AIAA Paper No. 2000-0548, Jan 10-13, 2000.

[10] Essick J. Advanced Labview Labs. Prentice Hall Inc., Upper Saddle River, NJ, 1999.

[11] Fox R. and McDonald A., Introduction to Fluid Mechanics. Fourth Edition. John Wiley & Sons, Inc. New York, 1992.

[12] Fukang Jiang, Yu-Chong Tai, Bhusan Gupta, Rodney Goodman, "A Surface-Micromachined Shear Stress Imager," UCLA and Caltech University, Los Angeles.

[13] Gad-el-Hak M. Flow Control. Passive, Active and Reactive Flow Management. Cambridge University Press, NY, 2000

[14] Gad-el-Hak M. "Flow Control," Applied Mechanics Review, Vol. 42: 261-292, 1989.

[15] Gad-el-Hak M. "Visualization Techniques for Unsteady Flows: An Overview." Journal of Fluids Engineering, Vol. 110: 231-243, 1988.

[16] Gad-el-Hak M. and Blackwelder R. F. "On the Growth of Turbulent Regions in Laminar Boundary Layers." Journal of Fluid Mechanics, Vol. 110: 73-95, 1981.

[17] Gad-el-Hak M. and Hussain F. A. K. M. "Coherent Structures in a Turbulent Boundary Layer. Part 1: Generation of 'Artificial" Bursts." Physics of Fluids, Vol. 29: 2124-2139, 1986.

[18] Hinze J. O. Turbulence. Second Edition. McGraw-Hill, Inc. New York, 1975.

[19] Ho C. M., "Control of Fluid Flows by Micro Transducers." UCLA, Los Angeles, CA 90095-1597.

[20] Ho C. M., Miu D., and Tai Yu-Chong, "Control of Macro Aerodynamic Device by Micro Actuators." UCLA and California Institute of Technology, Los Angeles.

[21] Ho C. M., Huang P. H., Yang J. M., Lee G. B., Tai Y. C., "Active Flow Control by MicroSystems." UCLA and California Institute of Technology, Los Angeles.

[22] Ho C. M, Tai Yu-Chong, "Micro-Electro-Mechanical-Systems (MEMS) and Fluid Flows." Annual Review of Fluid Mechanics, Vol. 30: 579-612, 1998.

[23] Huang L. and El-Genk M. S. "Heat Transfer and Flow Visualization Experiments of Swirling, Multi-Channel, and Conventional Impinging Jets," Int. J. Heat Mass Transfer, Vol. 41, No. 3: 583-600, 1998.

[24] Hughes, William F. and Brighton, John A. Fluid Dynamics Second Edition. McGraw-Hill, Inc. New York, 1991.

[25] King, L. V. *Phil. Mag.* Vol. 29: 556-577, 1915.

[26] Liu J. T. C. "Coherent Structures in Transitional and Turbulent Free Shear Flows." Ann. Rev. Fluid Mech. Vol. 21: 285-315, 1989.

[27] Lofdahl L. and Gad-el-Hak M., "MEMS-based Pressure and Shear Stress Sensors for Turbulent Flows." Measurement Science and Technology, Vol. 10: 665-686, 1999.

[28] Lumley J. and Blossey P. "Control of Turbulence." Annual Review of Fluid Mechanics, Vol. 30:311-327, 1998.

[29] Kuethe, Arnold M. and Chow, Chuen-Yen. Foundations of Aerodynamics, Bases of Aerodynamic Design, Fifth Edition. John Wiley & Sons, Inc. New York, 1998.

[30] Lin, Liwei and Yun, Weijie, "MEMS Pressure Sensors for Aerospace Applications," IEEE: 429-436, 1998.

[31] Liu J. T. C. "Coherent Structures in Transitional and Turbulent Free Shear Flows." Annual Review of Fluid Mechanics, Vol 21: 285-315, 1989.

[32] Mischler M., Tseng F., Ulmanella U., Ho C., "A Microsilicon Hot-Wire Anemometer." UCLA, Los Angeles.

[33] Morrison J. F., Subramanian C.S., and Bradshaw P., "Bursts and the Law of the Wall in Turbulent Boundary Layers," J. Fluid Mech. Vol. 241: 75-108, 1992.

[34] Myose R. Y. and Blackwelder R. F. "On the Role of the Outer Region in the Turbulent-Boundary-Layer Bursting Process," J. Fluid Mech. Vol. 259: 345-373, 1994.

[35] Offen G. R. and Kline S. J. "A Proposed Model of the Bursting Process in Turbulent Boundary Layers," J. Fluid Mechanics. Vol. 70: 209-228, 1975.

[36] Prosser S. J., "Advances in Sensors for Aerospace Applications," Sensors and Actuators, Vol. A37-38: 128-134, 1993.

[37] Saffman, P. G., Vortex Dynamics. Cambridge University Press, NY, 1992.

[38] Sherman F., Tung S., Chang-Jin, Ho C., Woo J. "Flow Control by Using High-Aspect-Ration, In-plane Microactuators," Mechanical and Aerospace Engineering Department, UCLA.

[39] Swearingen J. D. and Blackwelder R. F.,

[40] Tsao T., Jian F., Liu C., Miller R., Tung S., Huang J.-B., Gupta B., Babcock D., Lee C., Tai Y.-C., Ho C.-M., Kim J., and Goodman R., "MEMS-Based Active Drag Reduction in Turbulent Boundary Layers." UCLA, Los Angeles, and Caltech University, Pasadena, CA.

[41] White F. M. Viscous Fluid Flow, Second Edition. McGraw-Hill, Inc., New York, 1991.

[42] Wise K. D. "Micromechanical Sensors, Actuators and Systems." ASME Vol. 32, 1991.

[43] IFA 300 Constant Temperature Anemometer System Instruction Manual. TSI.

9. APPENDIX

9.1. APPENDIX A

Figure A.1 is a conversion chart of inches of water to velocity. This chart was used to convert the manometer reading into wind tunnel speed. The area error ratio used to correct the conversions was $A_2^2 : A_1^2 = 1:16$.

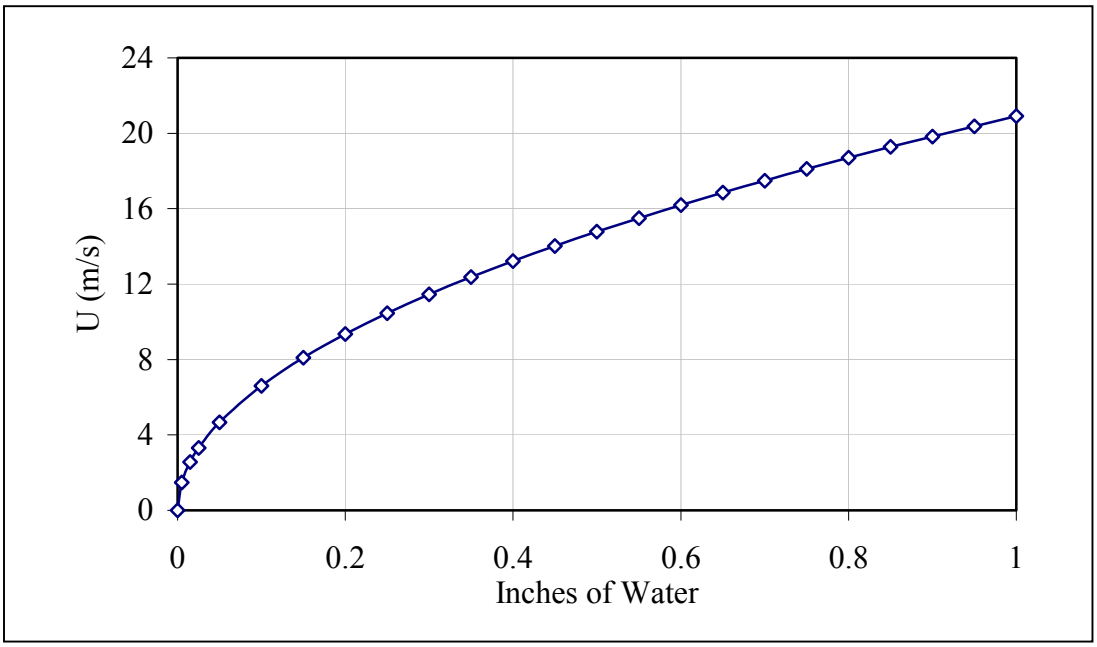

Figure A.1. Velocity Versus Inches of Water.

9.2. APPENDIX B

The following Figures are raw data files taken by the IFA 300 Anemometer System with the array of eight sensors. Each data plot shows different experimental parameters, the freestream velocity, U_{oo}, the actuation time, Ta, the downstream distance from the trailing edge of the piezoelectric actuator, x, and the height of the probe from the flat plate, y. For Figures B.2, B.3, B.4 and B.5, the data from all eight probes is shown. In Figure B.1, the data for probes 1, 2, 3, 4, 5, 7, and 8 are shown.

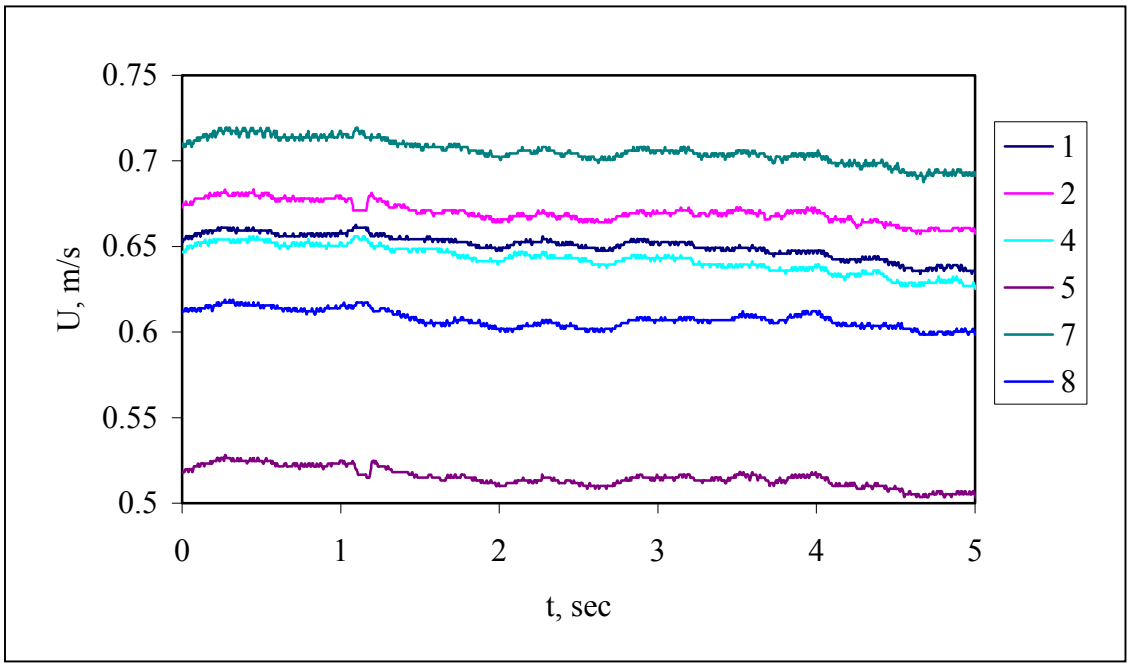

Figure B.1. Raw Data File, $U_\infty = 1.5\,\text{m/s},\ y = 3.0\,\text{mm},\ T_a = 0.1\,\text{sec},$
$3.0 \le x \le 12.0\,\text{mm}.$

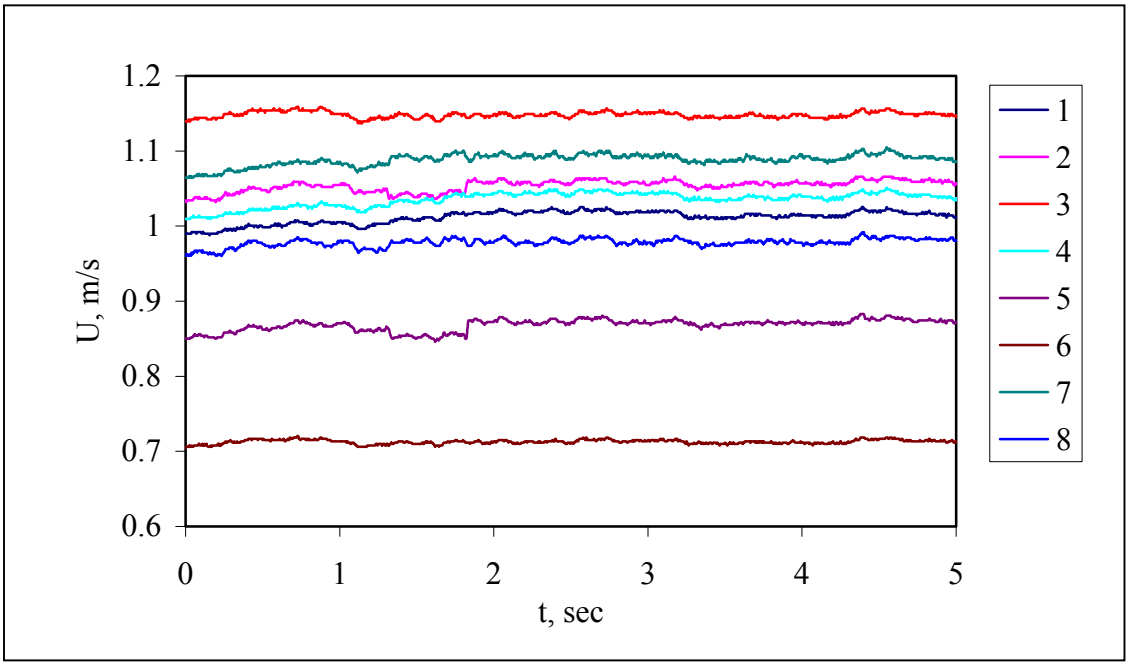

Figure B.2. Raw Data File, $U_\infty = 2.0$ m/s, $y = 2.0$ mm, $T_a = 0.5$ sec, $26.0 \le x \le 40.0$ mm.

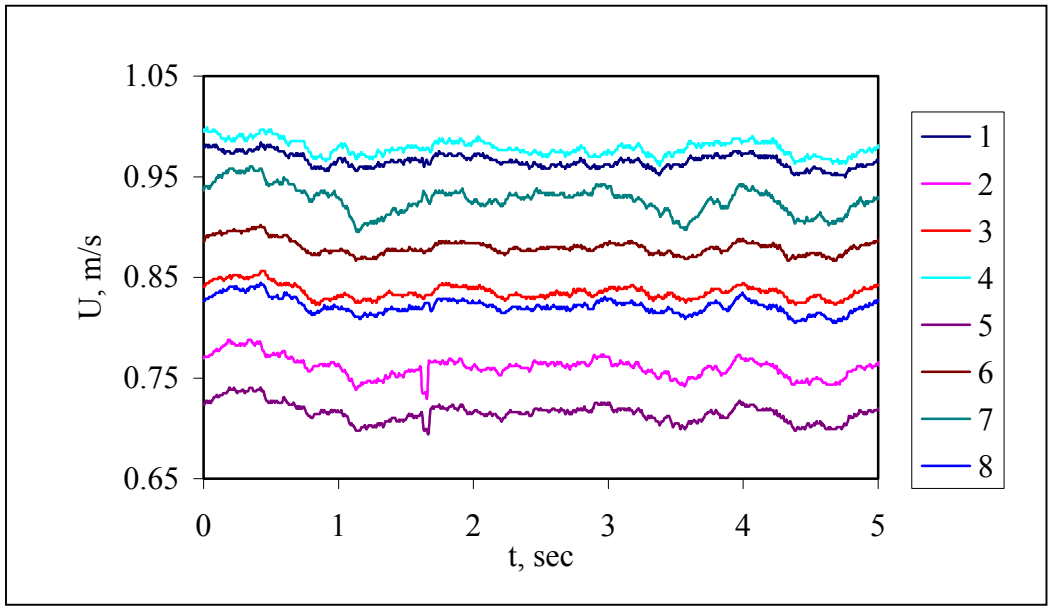

Figure B.3. Raw Data File, $U_\infty = 2.0$ m/s, $y = 2.0$ mm, $T_a = 0.05$ sec, $26.0 \le x \le 40.0$ mm.

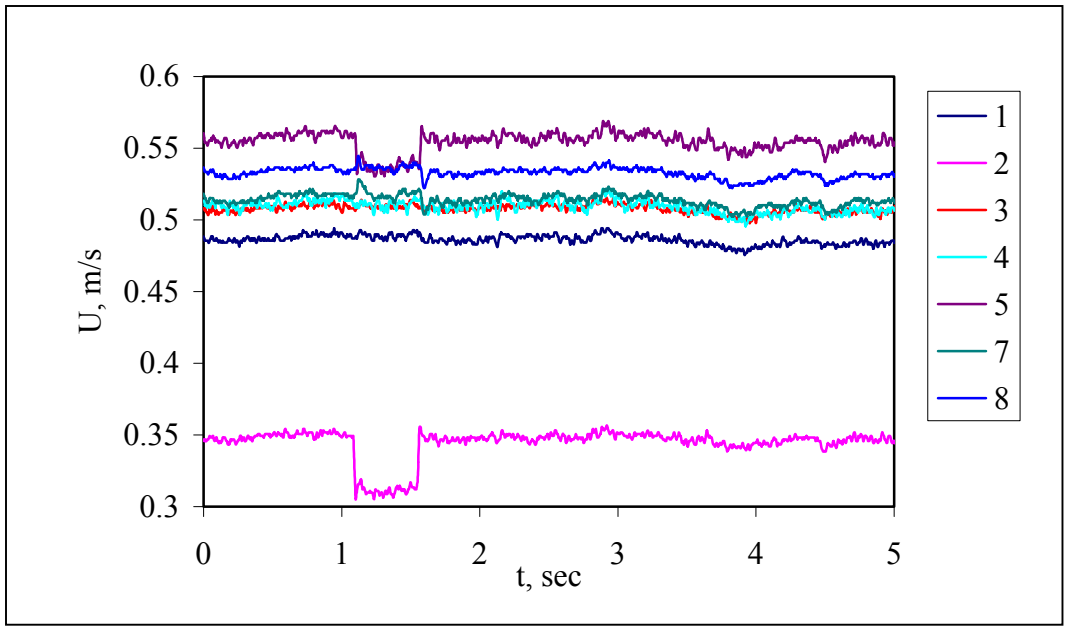

Figure B.4. Raw Data File, $U_\infty = 1.5\,\text{m/s},\ y = 1.0\,\text{mm},\ T_a = 0.5\,\text{sec},\ 3.0 \le x \le 12.0\,\text{mm}.$

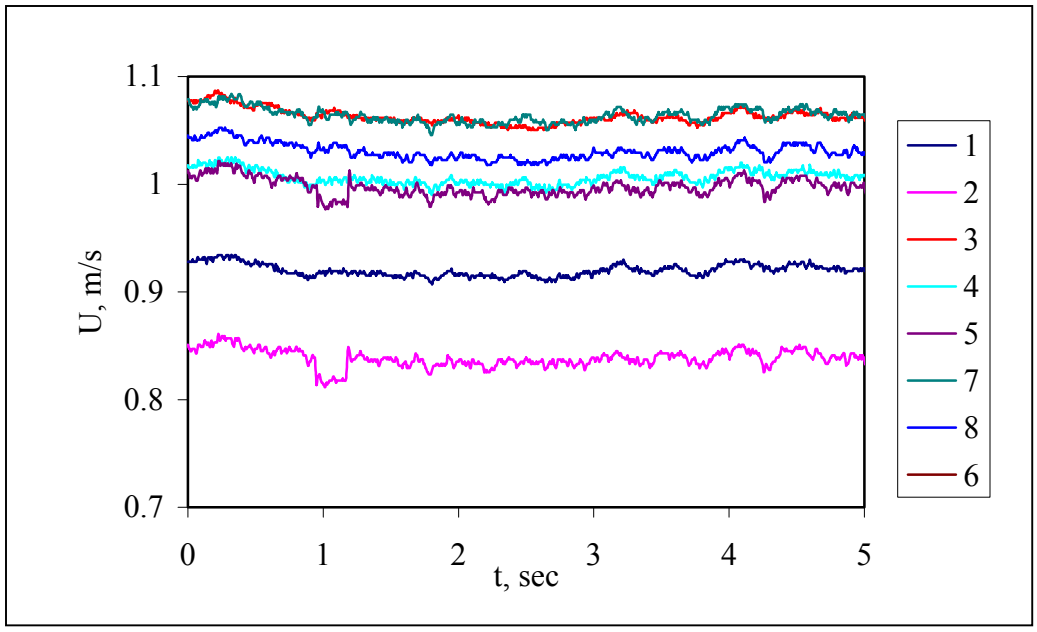

Figure B.5. Raw Data File, $U_\infty = 2.0\,\text{m/s},\ y = 3.0\,\text{mm},\ T_a = 0.25\,\text{sec},$
$3.0 \le x \le 12.0\,\text{mm}.$

9.3. APPENDIX C

This section contains a description of equipment set-up. Inside the computer is the LabView 6.0 Data Acquisition Card, which connects with the BNC 2080 hardware. This connects to the input of the ACX Amplifier. The ACX Amplifier output is connected to the piezoelectric bimorph actuator. Figure C.1 shows a schematic of the tutorial.

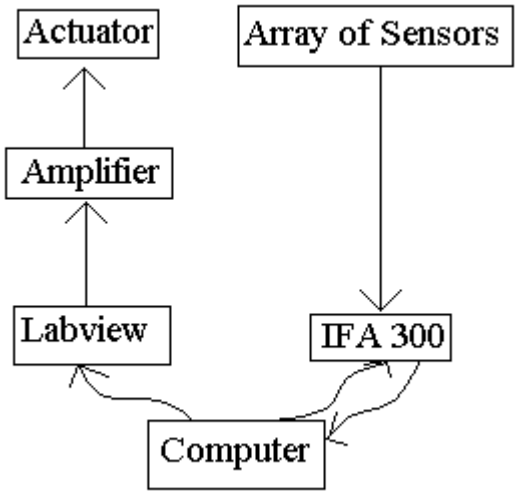

Figure C.1. Equipment Set-up Schematic.

The IFA 300 CTA system also connects to the computer. The output voltage ports are connected to a DAQ card within the computer. The probe connectors attach to the eight probe input ports.